nature communications

Article

https://doi.org/10.1038/s41467-023-37295-1

Quantum structural fluxion in superconducting lanthanum polyhydride

Received: 29 November 2022

Accepted: 9 March 2023

Published online: 25 March 2023

Check for updates

Hui Wang[1,2] ✉, Pascal T. Salzbrenner[3], Ion Errea[4,5,6], Feng Peng[7], Ziheng Lu[3], Hanyu Liu[2,8], Li Zhu[9], Chris J. Pickard[3,10] & Yansun Yao[11]

The discovery of 250-kelvin superconducting lanthanum polyhydride under high pressure marked a significant advance toward the realization of a room-temperature superconductor. X-ray diffraction (XRD) studies reveal a non-stoichiometric $LaH_{9.6}$ or $LaH_{10\pm\delta}$ polyhydride responsible for the superconductivity, which in the literature is commonly treated as LaH_{10} without accounting for stoichiometric defects. Here, we discover significant nuclear quantum effects (NQE) in this polyhydride, and demonstrate that a minor amount of stoichiometric defects will cause quantum proton diffusion in the otherwise rigid lanthanum lattice in the ground state. The diffusion coefficient reaches ~10^{-7} cm^2/s in $LaH_{9.63}$ at 150 gigapascals and 240 kelvin, approaching the upper bound value of interstitial hydrides at comparable temperatures. A puzzling phenomenon observed in previous experiments, the positive pressure dependence of the superconducting critical temperature T_c below 150 gigapascals, is explained by a modulation of the electronic structure due to a premature distortion of the hydrogen lattice in this quantum fluxional structure upon decompression, and resulting changes of the electron-phonon coupling. This finding suggests the coexistence of the quantum proton fluxion and hydrogen-induced superconductivity in this lanthanum polyhydride, and leads to an understanding of the structural nature and superconductivity of nonstoichiomectric hydrogen-rich materials.

Superconductivity at near room temperature has been discovered in clathrate polyhydrides at megabar pressures[1–7]. Determining the crystal structure responsible for the superconductivity is of critical importance, yet a great challenge[8,9]. Experimentally, difficulties in probing lighter elements arise in XRD, impeding a direct determination of the complete lattice symmetry. The measured T_c and its pressure dependence (dT_c/dp) tighten constraints on structural models; however, calculations on the candidate structures based on Bardeen–Cooper–Schrieffer (BCS) theory[10] unequivocally suggest a negative dT_c/dp[11–20], which contradicts the experimentally observed

[1]Key Laboratory for Photonic and Electronic Bandgap Materials (Ministry of Education), School of Physics and Electronic Engineering, Harbin Normal University, 150025 Harbin, China. [2]International Center for Computational Method & Software, College of Physics, Jilin University, 130012 Changchun, China. [3]Department of Materials Science & Metallurgy, University of Cambridge, 27 Charles Babbage Road, Cambridge CB3 0FS, UK. [4]Fisika Aplikatua Saila, Gipuzkoako Ingeniaritza Eskola, University of the Basque Country (UPV/EHU), Europa Plaza 1, 20018 Donostia/San Sebastián, Spain. [5]Centro de Física de Materiales (CSIC-UPV/EHU), Manuel de Lardizabal Pasealekua 5, 20018 Donostia/San Sebastián, Spain. [6]Donostia International Physics Center (DIPC), Manuel de Lardizabal Pasealekua 4, 20018 Donostia/San Sebastián, Spain. [7]College of Physics and Electronic Information, Luoyang Normal University, 471022 Luoyang, P. R. China. [8]State Key Laboratory of Superhard Materials and International Center of Future Science, Jilin University, 130012 Changchun, China. [9]Department of Physics, Rutgers University, Newark, NJ 07102, USA. [10]Advanced Institute for Materials Research, Tohoku University 2-1-1 Katahira, Aoba, Sendai 980-8577, Japan. [11]Department of Physics and Engineering Physics, University of Saskatchewan, Saskatoon, Saskatchewan S7N 5E2, Canada. ✉e-mail: wh@fysik.cn

positive dT_c/dp in some pressure regimes (Supplementary Fig. 1). This phenomenon was initially observed in the 250-kelvin superconducting lanthanum polyhydride[1], and later in polyhydrides of yttrium[6,7] and calcium[21] with T_c reaching 257 K and 212 K, respectively. This 'positive dT_c/dp contradiction' presents a major obstacle to our full understanding of the crystal structures of these superconducting polyhydrides.

As the first superconductor with a T_c above 250 K, lanthanum polyhydride has been studied by several groups independently[1–5]. In addition to the high T_c, a positive dT_c/dp was observed between 137 and 150 GPa by measurements on four samples (samples 1–4 in Ref. [1]) synthesized at different pressures with laser heating. XRD measurements determine that the lanthanum atoms form a face-centered cubic (*fcc*) lattice at pressures of 137–218 GPa, while the hydrogen atoms have undetermined locations within the lattice. Based on the measured crystal volume, the hydrogen-to-lanthanum (H/La) ratio around the maximum T_c was estimated to be 9.6 (150 GPa)[1] or 9–11 (180–200 GPa)[2,3] in the two studies, respectively. This trend was recently confirmed by new experiments on the *fcc* → *C*2/*m* phase transformation at $p_c = 135$ GPa, which shows an even steeper decrease of T_c below p_c[5].

With a moderate synthetic pressure and high symmetry, '*fcc*' lanthanum polyhydride provides a model system for exploring the structural nature of high-T_c hydrides in both experiment and theory. In fact, ab initio calculations have guided the experimental discovery of lanthanum polyhydrides, and predicted the appearance of high T_c superconductivity, i.e., an estimated T_c of 280-kelvin for *fcc*-LaH_{10} at 210 GPa[11,12]. This prediction turned out to be very close to the *fcc* lanthanum polyhydride later synthesized, with some differences in T_c, synthetic pressure, and hydrogen content. Recently, it has been theorized that the inclusion of quantum atomic fluctuation is essential for a correct calculation of T_c and the pressure boundary of *fcc*-LaH_{10}, which is dictated by the quantum nature of lanthanum polyhydride structures[16]. However, a negative dT_c/dp predicted at 137–150 GPa[16] remains in contradiction to the experimental observations (Supplementary Fig. 1). This disagreement suggests that critical factors have been overlooked in previous calculations of superconductivity. In particular, the stoichiometric defect observed by experimental studies may play an important role in determining the structure and underlying superconductivity.

Results and discussion

Although minor in amount, defects in solid materials can strongly affect their properties. The thermodynamic stability of a defect in high-pressure solids as well as the relative stabilities of different defect structures can be evaluated by the defect formation enthalpy (H^f). As shown in Fig. 1a, the crystal structure of *fcc*-LaH_{10} is represented as the insertion of an 'H cube' into octahedral interstices of the fluorite-LaH_2 structure. In this model, we calculated the H^f for a vacancy defect either at a corner of the H cube (V_C) or at a tetrahedral interstice of the La lattice (V_T), and found that the configurationally averaged H^f becomes negative below 158 GPa. This suggests that *fcc*-LaH_{10} is prone to vacancy defects, which agrees well with the experimental finding of hypostoichiometric $LaH_{10-\delta}$ at 150 GPa specifically $LaH_{9.6}$[1]. Notably, the calculated 'vacancy occurring region' coincides the region where the T_c of the *fcc* lanthanum polyhydride depends positively on the pressure (which previous calculations have failed to predict), indicating that the vacancy structure has a key role to play in the superconductivity.

A low concentration of vacancies in hydrogen sites does not change the XRD pattern of the *fcc* lanthanum polyhydride, which is determined primarily by the La sublattice. However, these vacancies significantly affect the dynamics of hydrogen in the crystal (Supplementary Fig. 2). The distortion in the hydrogen sublattice spreads out away from the vacancy sites in both the V_C and V_T models of LaH_{10} with an H/La ratio of 9.97, and even results in a 'liquid-like' H framework in

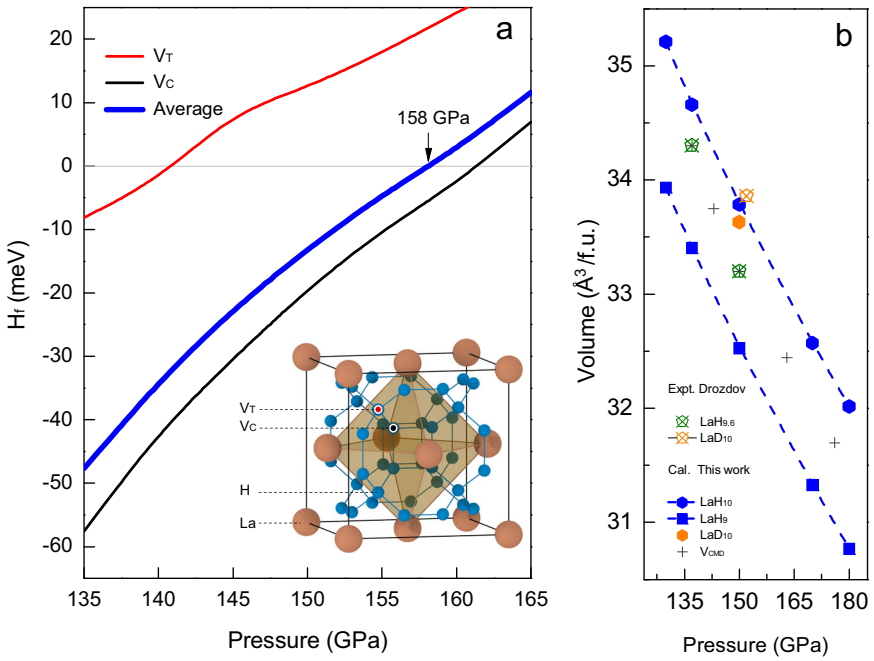

Fig. 1 | Vacancy formation enthalpy and pressure-volume relation. a The formation enthalpy (H_f) of a single vacancy in *fcc*-LaH_{10} at two inequivalent lattice sites in the clathrate hydrogen framework, V_T and V_C, and their configurational average calculated at different pressures using 2 × 2 × 2 extension of conventional unit cell of *fcc*-LaH_{10}. The locations of V_T and V_C are illustrated in a conventional unit cell of the *fcc*-LaH_{10} structure by red and black balls, respectively. **b** The experimental pressure-volume relations of *fcc*-$LaH_{9.6}$ and *fcc*-LaD_{10} measured by Drozdov et al.[1] compared to the theoretical values of *fcc*-LaH_{10}, *fcc*-LaH_9 and *fcc*-LaD_{10} derived from quantum simulations at constant pressure and temperature of 300 K. The volumes selected for subsequent quantum simulation (V_{CMD}) for *fcc*-$LaH_{9.63}$ are thereby linked to the 'quantum' pressure. Formula unit is abbreviated as f.u.

the former at 150 GPa. For $LaH_{10-\delta}$, the presence of vacancies changes the potential energy surface, while quantum nuclear fluctuation is expected to affect the transport behavior of vacancies. The calculated zero-point energy (ZPE) of ~150 meV/LaH_{10} is comparable to the vacancy migration energy of 160/200 meV for the migration path of $V_C \rightarrow V_C/V_C \rightarrow V_T$ at 150 GPa. This suggests that nuclear zero-point motion can promote proton hopping to neighboring vacancies and cause the $LaH_{10-\delta}$ ground state to not be a single structure around which the atoms vibrate, but instead one where the protons dynamically explore different vacancies in a fixed *fcc*-La framework.

We refer to this behavior as being 'fluxional' in the sense used by Goncharov et al. for phase IV of solid hydrogen[22]. It is well-established by experiment and theory that thermal effects dominate the fluxionality in this structure: A classically ordered phase III replaces the fluxional phase IV at low temperature[23–25]. Here, we demonstrate that, in the presence of vacancies, hydrogen NQEs are strong enough—and indeed essential—to stabilize a fluxional framework in the *fcc* lanthanum polyhydride. Therefore, we are dealing with a quantum fluxional structure (QFS).

Taking $LaH_{9.63}$ as an example, we investigate the NQE and thermal effects on the structural fluxion at 150 GPa and low temperatures up to 240 K. The stoichiometry is selected according to the experimental estimation ($LaH_{9.6}$). Our theoretical simulations suggest a H/La ratio of 9.54 (or 9.71) for the experimental samples synthesized at 150 GPa (or 137 GPa), in good agreement with experiments[1] (Fig. 1b). We adopt ab initio centroid molecular dynamics (CMD)[26] to treat the nuclei quantum mechanically. As shown by the mean square displacement (MSD) curves in Fig. 2a, the simulations reveal appreciable proton migration, with equivalent mean migration distances of vacancies reaching 1.0 to 2.0 Å between 60 and 240 K (Supplementary Fig. 3). These distances are almost as large as or larger than the shortest H-H separation around 1.2 Å. This is consistent with the 'network'-like density distribution patterns obtained, for instance, at 60 K (Fig. 2b). In contrast, the diffusivity is much smaller in ab initio molecular dynamics (MD), where the nuclei are treated classically (Fig. 2a, c). This confirms that the structural fluxion in $LaH_{9.63}$ is dominated by the NQE, rather than thermal effects. The crucial role of vacancies in this intriguing quantum phenomenon is demonstrated by a comparison to the dynamics of stoichiometric *fcc*-LaH_{10} at the same pressure, which exhibits no diffusion below 700 K[27]. Experimentally, the occurrence of 'quenched-in' vacancies in polyhydrides is inevitable, as a result of the thermal treatment of the samples. This finding therefore suggests that vacancy effects interact with the strong NQE to result in strong quantum structural fluxion in polyhydrides.

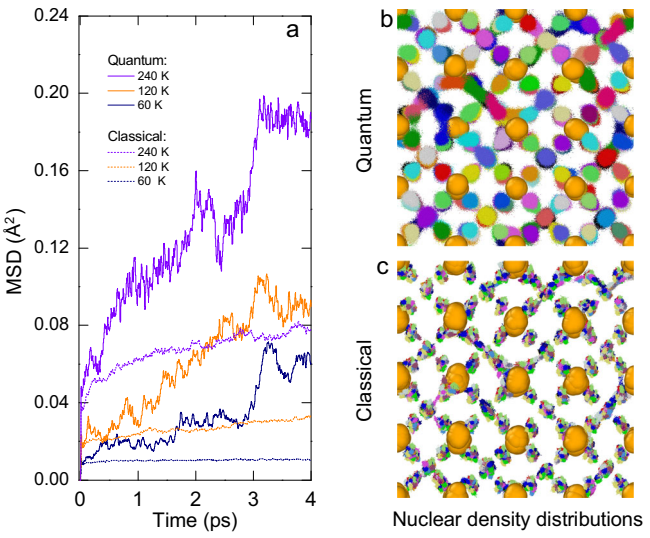

Fig. 2 | Structural fluxion in $LaH_{9.63}$ at 150 GPa. a The proton MSD derived from centroid trajectories of the CMD simulations and those of MD simulations. **b** The [100] view of the quantum nuclear density distribution at 60 K extracted from a CMD simulation, with full consideration of the 16 beads. Neighboring protons are illustrated in different colors. **c** the [100] view of the classical nuclear density distribution in 16 MD simulation runs of 4 ps distinguished by various proton colors. The 16 runs were initialized from different centroid configurations of the 4-picosecond CMD trajectory with a sampling interval of 0.25 ps.

We approximate the proton diffusion coefficient D in $LaH_{9.63}$ from the slope of the MSD in simulations at 240 K and between 137 to 176 GPa. The temperature is chosen to be close to the measured T_c of the *fcc* lanthanum polyhydride. As shown in Fig. 3a, the D value falls in the range of 10^{-6} to 10^{-7} cm²/s in our quantum simulation, whereas it is significantly lower in the classical simulation. The D value is 2–3 orders of magnitude below the threshold criterion for classical superionicity (~10^{-4} cm²/s) for freely diffusing protons[28]. This notwithstanding, it reaches or indeed exceeds the upper bound diffusivities observed in interstitial hydrides at room temperature, such as 3.8×10^{-7} cm²/s in *fcc*-Cu_2H[29], and approaches that of phase IV hydrogen[30]. With increasing pressure, D decreases in interstitial hydrides (e.g. Cu_2H[29] and FeH[31]), due to the contraction of the metal lattice and the resulting increase of the activation energy for proton hopping. In phase IV hydrogen, on the other hand, D increases with pressure[30], probably owing to the drastic increase of the proton hopping rate with the shortened of the distance. Our preliminary results suggest that the unique 'host-guest' structure of $LaH_{9.63}$ likely induces a significant competition between the two mechanisms mentioned, resulting in a nonmonotonic pressure trend of the coefficient D.

In $LaH_{9.63}$, proton diffusion breaks the balance of internal Coulomb repulsions in the 'H cube' located in octahedral interstices of La sublattice, which therefore distorts the H sublattice. Lattice expansion promotes the distortion, as indicated by the heightening of the second coordination shell (peaked at ~1.85 Å) in the average radial distribution function [RDF, g(r), Supplementary Fig. 4], which is correlated to a smearing of the inter- and inner-cube H-H separations. Based on a configurational distance (denoted as ξ) of crystal fingerprint matrices[32], which is sensitive to local structural changes, we parametrized the structural difference of the QFS relative to the crystal lattices of static *fcc* and *C*2/*m* phases, and a triclinic *P*1 structure mimicking the QFS, as shown in Fig. 3b by ξ_{qf}, ξ_{qc} and ξ_{qp} respectively. For the H substructure, we find $\xi_{qf} > \xi_{qc} > \xi_{qp}$, with the ξ_{qf} much beyond the other two at larger volumes, revealing an increasing distortion of the H sublattice in QFS from *fcc* to lower symmetry upon decompression. For the La substructure, $\xi_{qc} > \xi_{qf} \approx \xi_{qp}$, with ξ_{qc} much larger than ξ_{qf} and ξ_{qp}. This agrees with the XRD measurements that determine an *fcc* sublattice for La atoms above 137 GPa[1]. The tiny distortions related to ξ_{qf} and ξ_{qp} are both within the uncertainty of refinements for the *fcc* phase in XRD studies (Supplementary Fig. 4). The results suggest a premature low-symmetry distortion of the H substructure upon volume expansion relative to the La substructure in the quantum fluxional $LaH_{9.63}$.

Using the centroid configurations of CMD simulations at 240 K, i.e. the QFS, we calculated the electronic density of states at the Fermi level $N(\epsilon_F)$ in $LaH_{9.63}$, which exhibits opposite pressure trends at pressure below and above 150 GPa (Fig. 4a). The *fcc*-LaH_{10} (quantum) crystal has a monotonously negative pressure dependence of $N(\epsilon_F)$ above 100 GPa[12,16], and this prediction can be extended to $LaH_{9.63}$ using the rigid-band model of the electronic structure by virtue of an artificial shift of ϵ_F[33]. The pressure dependences of $N(\epsilon_F)$ in the *C*2/*m* phase of LaH_{10} and $LaH_{9.63}$ (within the rigid-band approximation) are both non-monotonic, similar to quantum fluxional $LaH_{9.63}$, suggesting that pressure effects on $dN(\epsilon_F)/dp$ are much more significant in distorted structures compared to the high-symmetry *fcc* phase. The non-monotonic pressure trend of $N(\epsilon_F)$ in $LaH_{9.63}$ is a statistical consequence of the QFS having an average *fcc*-La sublattice with diversely distorted H substructures. This trend cannot be attributed to a single classical configuration, but can roughly be reproduced by the *P*1 structure mimicking the QFS

https://doi.org/10.1038/s41467-023-37295-1

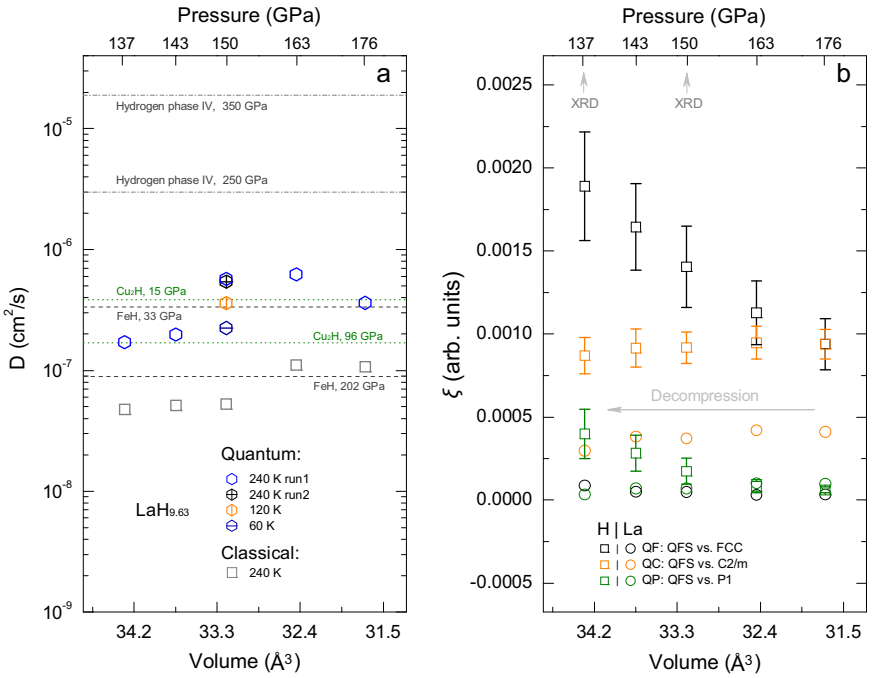

Fig. 3 | Pressure effects on the diffusivity and structural distortions. a The proton diffusion coefficient D derived from the MSD in CMD simulations (run1) of 4 ps, and from the average MSD of four MD simulations of 24 ps. The D in three additional CMD simulations of 4 ps at 150 GPa are also shown. These are two simulations at 120 K and 60 K, and a simulation using higher total-energy convergence criteria (run2). The MSD in the CMD simulations is derived from the centroid trajectories. The measured D in Cu_2H[29] and FeH[31], and calculated D in phase IV hydrogen[30] are shown for comparison. **b** The configurational distance ξ (with error bar indicating the standard deviation) of QFS from the crystal lattices of static *fcc* and *C*2*m* phases, and a triclinic *P*1 structure for H and La substructure. The *P*1 structure is built by scaling the lattice parameter a of a QFS sampled from the CMD simulation of $LaH_{9.63}$ at 176 GPa.

(Supplementary Fig. 5), which implies that the premature distortion of the H substructure (e.g. *fcc* → *P*1 symmetry) accounts for the sign change of $dN(\epsilon_F)/dp$ in the quantum fluxional $LaH_{9.63}$.

The analytic McMillan[34] and Allen-Dynes (AD)[35] formulas (see details in Supplemental Information) have played an important role in analyzing the mechanism of pressure-dependent superconductivity in high-T_c hydrides. In these formulas, the electron-phonon coupling (EPC) constant λ depends explicitly on characteristic parameters of both electrons and phonons, in addition to the average of the electron-phonon matrix elements, $\langle I^2 \rangle$. Specifically, λ can be expressed as the product of $\langle I^2 \rangle / M$ (denoted as β, with M being atomic mass) and $N(\epsilon_F)/(\bar{\omega}_2^2)$ (denoted as ζ, with $\bar{\omega}_2$ being the second frequency moment of the Eliashberg function). ζ directly describes the competition between electron and phonon contributions. Analysis of literature data suggest that ζ decreases more than two times faster than β increases upon compression (Supplementary Table 1). Furthermore, it was found that $d\lambda/dp$ plays a dominating role in determining the dT_c/dp, despite the fact that the T_c also depends explicitly on ω_{log} and $\bar{\omega}_2/\omega_{log}$ (with ω_{log} being the logarithmic frequency moment of the Eliashberg function). These findings suggest two rules for single crystal phases of high-T_c hydrides: (I) phonons affect dT_c/dp mainly through the parameter λ; and (II) $d\lambda/dp$ is primarily determined by $d\zeta/dp$, rather than $d\beta/dp$.

In view of ζ being proportional to $N(\epsilon_F)$, the pressure trend of $N(\epsilon_F)$ in $LaH_{9.63}$ (Fig. 4a) suggests a sign change of dT_c/dp at studied pressures. Since the quantum fluxional nature of $LaH_{9.63}$ forbids a direct calculation of the Eliashberg function $\alpha(\omega)^2F(\omega)$ by density functional methods, a quantitative confirmation of this is unachievable yet. However, considering that the change is so significant that even qualitative estimations could provide insights, we study the sign of dT_c/dp slope in $LaH_{9.63}$ under two approximations, as the first step to access the problem: (I) calculating ω_{log} and $\bar{\omega}_2$ based on the phonon spectrum $F(\omega)$ of $LaH_{9.63}$, combined with $\alpha(\omega)^2$ approximated by that of quantum *fcc*-LaH_{10}; (II) approximating the β in $LaH_{9.63}$ by that of the quantum *fcc*-LaH_{10}. The rationale of such approximation is based on empirical rules, and the fact that quantum fluxional $LaH_{9.63}$ largely retains the same local atomic environment as quantum *fcc*-LaH_{10} (Supplementary Fig. 6). The $F(\omega)$ derived from the Fourier transform of the velocity autocorrelation functions in the CMD simulations at 240 K, as well as the approximated $\alpha(\omega)^2$ and $\alpha(\omega)^2F(\omega)$ are shown in Supplementary Fig. 7.

With this approach, we evaluated the pressure trend of T_c in $LaH_{9.63}$ using the AD formula (with parameters listed in Supplementary Table 2). It does indeed exhibit a positive dT_c/dp slope at 137–163 GPa, in qualitative agreement with experimental observation[1] (Fig. 4b). Moreover, a negative dT_c/dp slope is obtained at higher pressures in line with both experimental observations and theoretical results for *fcc*-LaH_{10} (Supplementary Fig. 1). The standard deviation of $N(\epsilon_F)$ (Supplementary Fig. 5) reveals fluctuations of the electron structure near the Fermi level, which may affect the T_c through parameters ζ and λ. However, considering that superconductivity of $LaH_{9.6}$ is measured at a time scale far beyond that of the simulation, it is feasible to calculate the T_c by a averaged $N(\epsilon_F)$. Recently, the *C*2/*m* phase has been successfully prepared at 120 GPa by abrupt decompression of the *fcc* phase[5]. A positive dT_c/dp slope measured in the subsequent compression was attributed to a boost in the T_c due to phonon softening. As illustrated in the literature[12,16], the softening of phonons results in a negative dT_c/dp slope for *fcc*-LaH_{10}, in contrast to the experimental observations below 150 GPa[1]. However, the concept of 'a higher T_c near structural instability'[5] agrees well with our finding of a premature distortion of hydrogen substructure relative to an average *fcc*-La substructure in quantum fluxional $LaH_{9.63}$, upon decompression to 137 GPa.

In summary, the present work illustrates in lanthanum polyhydride the coexistence of quantum proton fluxion and hydrogen-induced high-T_c superconductivity. A premature distortion of hydrogen substructure upon volume expansion and its impact on the superconductivity through modulating the electronic structure is revealed. The findings

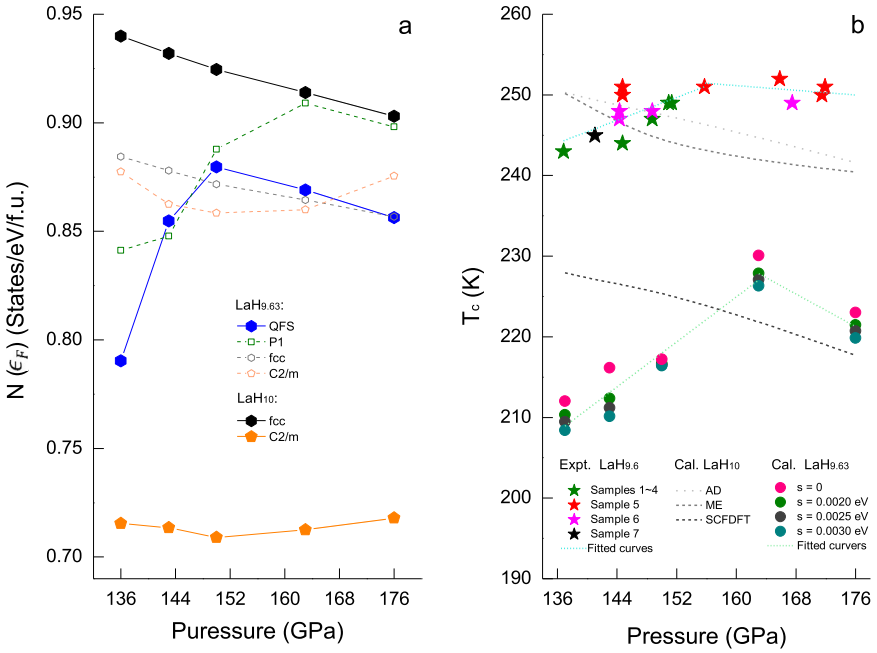

Fig. 4 | Pressure effects on electronic properties and superconductivity. a The pressure trend of the averaged electronic density of states at the Fermi level $N(\epsilon_F)$ in quantum fluxional $LaH_{9.63}$ (with distributions and standard deviation of statics shown in Supplementary Fig. 5), and the pressure trend of $N(\epsilon_F)$ in static *P*1-$LaH_{9.63}$, *fcc*-LaH_{10}, and *C*2/*m*-LaH_{10}. The $N(\epsilon_F)$ of $LaH_{9.63}$ in *fcc* and *C*2/*m* phase estimated using the rigid-band approximation are also shown for comparison. **b** The pressure trend of T_c in quantum fluxional $LaH_{9.63}$ calculated based on various Gaussian smearings (σ) of the phonon spectrum $F(\omega)$, together with the values measured for $LaH_{9.6}$ by Drozdov et al.[1] and those derived from AD, Migdal–Eliashberg equations (ME), and superconducting DFT (SCDFT) for *fcc*-LaH_{10} by Errea et al.[16]. Fitted lines are shown to guide the sight.

support the experimental argument concerning the hypostoichiometric nature of the superconducting samples, reveal the crucial role of vacancy defects in the structure, and provide a theoretical explanation for the positive dT_c/dp slope of lanthanum polyhydride, with implications for understanding the structure and superconductivity of other hydrogen-rich materials. With significant progress of nuclear magnetic resonance techniques in diamond anvil cells, the measurement of proton mobility in metal hydrides is currently accessible at megabar pressures[29,31]. We anticipate that continuous experimental and theoretical studies of quantum fluxional structure of high-T_c hydrides will stimulate new theoretical tools for understanding the superconducting behavior of quantum fluxional materials that cannot be precisely described by a single underlying static structure.

Methods

The ab initio calculations were performed using the plane-wave pseudopotential method, as implemented in the Vienna ab initio simulation program (VASP)[36], with the Perdew–Burke–Ernzerhof (PBE) Generalized Gradient Approximation (GGA) density functional[37], and the bare ion Coulomb potential treated in the projector augmented wave (PAW) framework[38]. The vacancy formation enthalpy of *fcc*-LaH_{10} was calculated from vacancy structures of *fcc*-LaH_{10} and B_2/n-H_2[39], with enthalpies calculated using the third-order Birch–Murnaghan isothermal equation of state (EOS)[40] from ab initio energy-volume relations, as implemented in the EOS code[41]. The vacancy migration energy was calculated by the climbing image nudged elastic band method (CI-NEB)[42]. The quantum nuclear dynamics were studied by path-integral molecular dynamics (PIMD) and centroid molecular dynamics (CMD)[30], as implement in the PIMD code[43]. The superconductivity was analyzed using McMillan's theory[34] with the T_c estimated by the Allen-Dynes equations[35]. The crystal structures and MD trajectories were visualized by the VESTA[44] and OVITO softwares[45] respectively. More details are shown in the Supplementary Information.

Data availability

All data are available in the paper and from the author upon request.

References

1. Drozdov, A. P. et al. Superconductivity at 250 K in lanthanum hydride under high pressures. *Nature* **569**, 528–531 (2019).
2. Somayazulu, M. et al. Evidence for superconductivity above 260 K in lanthanum superhydride at megabar pressures. *Phys. Rev. Lett.* **122**, 027001 (2019).
3. Geballe, Z. M. et al. Synthesis and stability of lanthanum superhydrides. *Angew. Chem. Int. Ed.* **57**, 688–692 (2018).
4. Struzhkin, V. et al. Superconductivity in La and Y hydrides: remaining questions to experiment and theory. *Mat. Rad. Extr.* **5**, 028201 (2020).
5. Sun, D. et al. High-temperature superconductivity on the verge of a structural instability in lanthanum superhydride. *Nat. Commun.* **12**, 6863 (2021).
6. Snider, E. et al. Synthesis of yttrium superhydride superconductor with a transition temperature up to 262 K by catalytic hydrogenation at high pressures. *Phys. Rev. Lett.* **126**, 117003 (2021).
7. Kong, P. et al. Superconductivity up to 243 K in the yttrium-hydrogen system under high pressure. *Nat. Commun.* **12**, 5075 (2021).
8. Flores-Livas, J. A. et al. A perspective on conventional high-temperature superconductors at high pressure: Methods and materials. *Phys. Rep.* **856**, 1–78 (2020).
9. Pickard, C. J., Errea, I. & Eremets, M. I. Superconducting hydrides under pressure. *Annu. Rev. Condens. Matter Phys.* **11**, 57–76 (2020).
10. Bardeen, J., Cooper, L. N. & Schrieffer, J. R. Theory of superconductivity. *Phys. Rev.* **108**, 1175–1204 (1957).
11. Peng, F. et al. Hydrogen clathrate structures in rare earth hydrides at high pressures: possible route to room-temperature superconductivity. *Phys. Rev. Lett.* **119**, 107001 (2017).

12. Liu, H., Naumov, I. I., Hoffmann, R., Ashcroft, N. W. & Hemley, R. J. Potential high-T_c superconducting lanthanum and yttrium hydrides at high pressure. *Proc. Natl Acad. Sci. USA* **114**, 6990 (2017).
13. Liu, L. et al. Microscopic mechanism of room-temperature superconductivity in compressed LaH_{10}. *Phys. Rev. B* **99**, 140501 (2019).
14. Wang, C., Yi, S. & Cho, J.-H. Pressure dependence of the superconducting transition temperature of compressed LaH_{10}. *Phys. Rev. B* **100**, 060502 (2019).
15. Quan, Y., Ghosh, S. S. & Pickett, W. E. Compressed hydrides as metallic hydrogen superconductors. *Phys. Rev. B* **100**, 184505 (2019).
16. Errea, I. et al. Quantum crystal structure in the 250-kelvin superconducting lanthanum hydride. *Nature* **578**, 66–69 (2020).
17. Kruglov, I. A. et al. Superconductivity of LaH_{10} and LaH_{16} polyhydrides. *Phys. Rev. B* **101**, 024508 (2020).
18. Wang, H., Tse, J. S., Tanaka, K., Iitaka, T. & Ma, Y. Superconductive sodalite-like clathrate calcium hydride at high pressures. *Proc. Natl Acad. Sci. USA* **109**, 6463 (2012).
19. Xie, H. et al. High-temperature superconductivity in ternary clathrate $YCaH_{12}$ under high pressures. *J. Phys: Condens Matter* **31**, 245404 (2019).
20. Song, H. et al. High T_c superconductivity in heavy rare earth hydrides. *Chin. Phys. Lett.* **38**, 107401 (2021).
21. Ma, L. et al. High-temperature superconducting phase in clathrate calcium hydride CaH_6 up to 215 K at a pressure of 172 GPa. *Phys. Rev. Lett.* **128**, 167001 (2022).
22. Goncharov, A. F., Chuvashova, I., Ji, C. & Mao, H.-k Intermolecular coupling and fluxional behavior of hydrogen in phase IV. *Proc. Natl Acad. Sci. USA* **116**, 25512 (2019).
23. Howie, R. T., Guillaume, C. L., Scheler, T., Goncharov, A. F. & Gregoryanz, E. Mixed molecular and atomic phase of dense hydrogen. *Phys. Rev. Lett.* **108**, 125501 (2012).
24. Zha, C. et al. High-pressure measurements of hydrogen phase IV using synchrotron infrared spectroscopy. *Phys. Rev. Lett.* **110**, 217402 (2013).
25. Magdău, I. B. & Ackland, G. J. Identification of high-pressure phases III and IV in hydrogen: simulating Raman spectra using molecular dynamics. *Phys. Rev. B* **87**, 174110 (2013).
26. Shiga, M., Tachikawa, M. & Miura, S. A unified scheme for ab initio molecular orbital theory and path integral molecular dynamics. *J. Chem. Phys.* **115**, 9149–9159 (2001).
27. Liu, H. et al. Dynamics and superconductivity in compressed lanthanum superhydride. *Phys. Rev. B* **98**, 100102(R) (2018).
28. Katoh, E., Yamawaki, H., Fujihisa, H., Sakashita, M. & Aoki, K. Protonic diffusion in high-pressure ice VII. *Science* **295**, 1264 (2002).
29. Meier, T. et al. Proton mobility in metallic copper hydride from high-pressure nuclear magnetic resonance. *Phys. Rev. B* **102**, 165109 (2020).
30. Liu, H. & Ma, Y. Proton or deuteron transfer in phase IV of solid hydrogen and deuterium. *Phys. Rev. Lett.* **110**, 025903 (2013).
31. Meier, T. et al. Pressure-induced hydrogen-hydrogen interaction in metallic FeH revealed by NMR. *Phys. Rev. X* **9**, 031008 (2019).
32. Zhu, L. et al. A fingerprint based metric for measuring similarities of crystalline structures. *J. Chem. Phys.* **144**, 034203 (2016).
33. Boeri L. in *Handbook of Materials Modeling: Applications: Current and Emerging Materials* (eds Andreoni, W. & Yip, S.) (Springer International Publishing, 2018).
34. McMillan, W. L. Transition temperature of strong-coupled superconductors. *Phys. Rev.* **167**, 331–344 (1968).
35. Allen, P. B. & Dynes, R. C. Transition temperature of strong-coupled superconductors reanalyzed. *Phys. Rev. B* **12**, 905–922 (1975).
36. Kresse, G. & Furthmüller, J. Efficient iterative schemes for ab initio total-energy calculations using a plane-wave basis set. *Phys. Rev. B* **54**, 11169–11186 (1996).
37. Perdew, J. P., Burke, K. & Ernzerhof, M. Generalized gradient approximation made simple. *Phys. Rev. Lett.* **77**, 3865–3868 (1996).
38. Blöchl, P. E. Projector augmented-wave method. *Phys. Rev. B* **50**, 17953–17979 (1994).
39. Pickard, C. J. & Needs, R. J. Structure of phase III of solid hydrogen. *Nat. Phys.* **3**, 473–476 (2007).
40. Birch, F. Finite elastic strain of cubic crystals. *Phys. Rev.* **71**, 809–824 (1947).
41. Dewhurst, J. & Ambrosch-Draxl C. The EXCITING Code Users' Manual Version 0.9.74 (2021).
42. Henkelman, G., Uberuaga, B. P. & Jónsson, H. A climbing image nudged elastic band method for finding saddle points and minimum energy paths. *J. Chem. Phys.* **113**, 9901–9904 (2000).
43. Shiga, M., Tachikawa, M. & Miura, S. Ab initio molecular orbital calculation considering the quantum mechanical effect of nuclei by path integral molecular dynamics. *Chem. Phys. Lett.* **332**, 396–402 (2000).
44. Momma, K. & Izumi, F. VESTA3 for three-dimensional visualization of crystal, volumetric and morphology data. *J. Appl. Crystallogr.* **44**, 1272–1276 (2011).
45. Stukowski, A. Visualization and analysis of atomistic simulation data with OVITO-the Open Visualization Tool. *Model. Simul. Mater. Sci. Eng.* **18**, 015012 (2010).

Acknowledgements

H.W. is thankful to Y. Ma and M. Shiga for valuable discussions, to V. Minkov and M. Eremets for the XRD data, and to C.Wang for the EPC data. The project is supported by the National Natural Science Foundation of China (Grant No. 11974135, 11874176, 12174170, and 12074138), the Natural Sciences and Engineering Research Council of Canada, the EPSRC through grants EP/P022596/1, and EP/S021981/1, and the startup funds of the office of the Dean of SASN of Rutgers University-Newark. P. T. S. thanks the Department of Materials Science and Metallurgy at the University of Cambridge for generous funding. The work of P. T. S. is further supported through a Trinity Hall research studentship. I. E. acknowledges financial support by the European Research Council (ERC) under the European Union's Horizon 2020 research and innovation program (grant agreement no. 802533). We used the computing facilities at Beijing Super Cloud Computing Center.

Author contributions

H.W., P.S., I.E., F.P., Z.L., H.L., and L.Z. performed the calculations. H.W., Y.Y., P.S., and C.P. wrote the manuscript, with input from all co-authors.

Competing interests

The authors declare no competing interests.

Additional information

Supplementary information The online version contains supplementary material available at https://doi.org/10.1038/s41467-023-37295-1.

Correspondence and requests for materials should be addressed to Hui Wang.

Peer review information *Nature Communications* thanks the anonymous reviewers for their contribution to the peer review of this work. Peer reviewer reports are available.

Supplementary Information of

"Quantum structural fluxion in superconducting lanthanum polyhydride"

Hui Wang[1,2*], Pascal T. Salzbrenner[3], Ion Errea[4,5,6], Feng Peng[7], Ziheng Lu[3], Hanyu Liu[2,8], Li Zhu[9], Chris J. Pickard[3,10] and Yansun Yao[11]

[1]*Key Laboratory for Photonic and Electronic Bandgap Materials (Ministry of Education), School of Physics and Electronic Engineering, Harbin Normal University, Harbin 150025, China*

[2]*International Center for Computational Method & Software, College of Physics, Jilin University, Changchun 130012, China*

[3]*Department of Materials Science & Metallurgy, University of Cambridge, 27 Charles Babbage Road, Cambridge CB3 0FS, United Kingdom*

[4]*Fisika Aplikatua Saila, Gipuzkoako Ingeniaritza Eskola, University of the Basque Country (UPV/EHU), Europa Plaza 1, 20018 Donostia/San Sebastián, Spain*

[5]*Centro de Física de Materiales (CSIC-UPV/EHU), Manuel de Lardizabal Pasealekua 5, 20018 Donostia/San Sebastián, Spain*

[6]*Donostia International Physics Center (DIPC), Manuel de Lardizabal Pasealekua 4, 20018 Donostia/San Sebastián, Spain*

[7]*College of Physics and Electronic Information, Luoyang Normal University, Luoyang 471022, P. R. China*

[8]*State Key Laboratory of Superhard Materials and International Center of Future Science, Jilin University, Changchun 130012, China*

[9]*Department of Physics, Rutgers University, Newark, NJ 07102, USA*

[10]*Advanced Institute for Materials Research, Tohoku University 2-1-1 Katahira, Aoba, Sendai, 980-8577, Japan*

[11]*Department of Physics and Engineering Physics, University of Saskatchewan, Saskatoon, Saskatchewan S7N 5E2, Canada*

[*]e-mail: wh@fysik.cn

Table of contents

Supplementary Figure 1

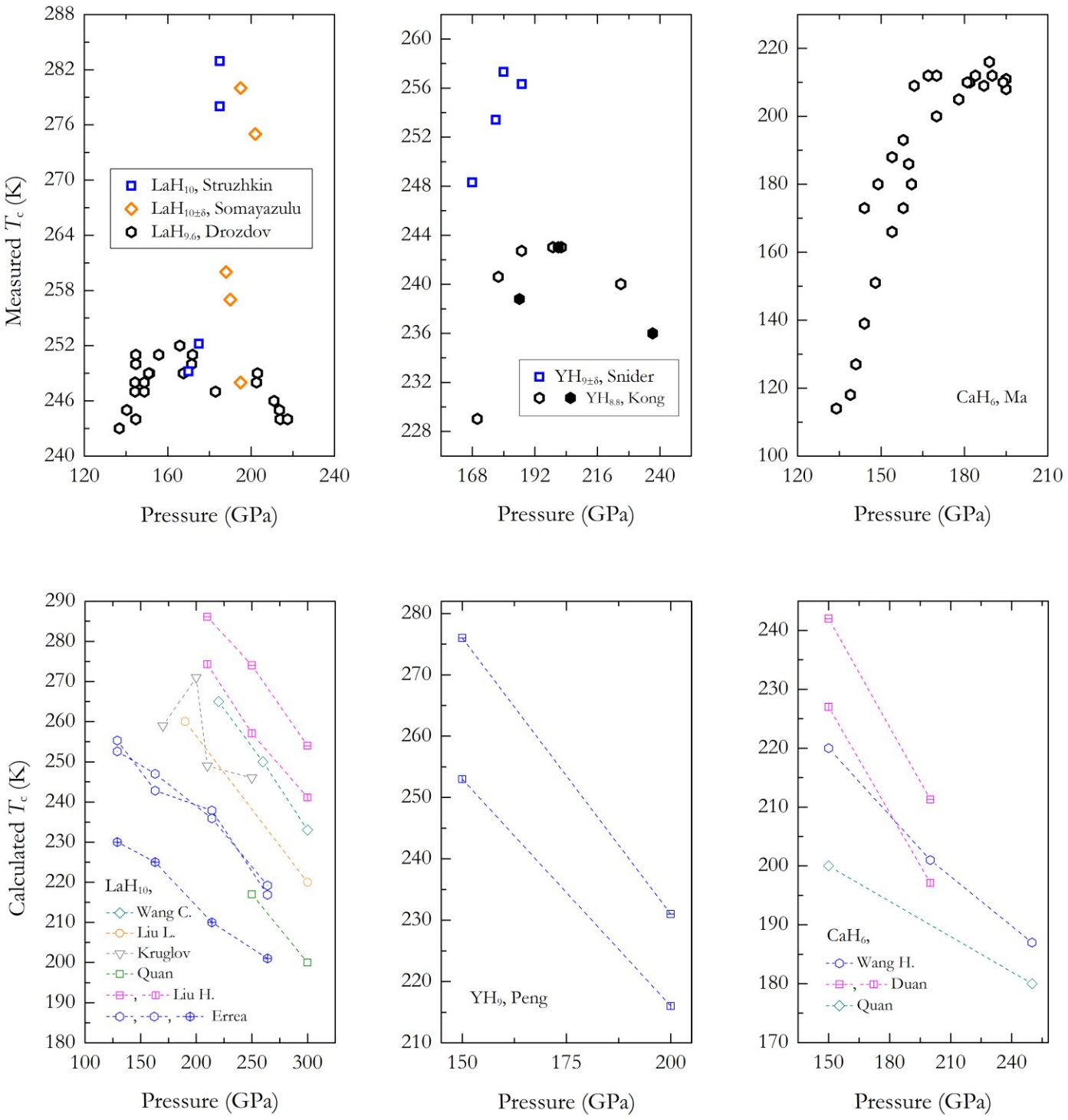

Supplementary Figure 1| The 'positive dT_c/dp contradiction'.

Recent experimental studies by Drozdov *et. al.*[1], Somayazulu *et. al.*[2], Struzhkin *et. al.*[3], Kong *et. al.*[4], Snider *et. al.*[5] and Ma *et. al.*[6] discovered several near-room temperature superconducting polyhydrides, and the measured pressure trend of T_c usually reveals a positive dT_c/dp at some pressure regimes, in contradiction with the negative slope predicted by earlier or subsequent calculations by Peng *et. al.*[7], Liu H. *et. al.*[8], Liu L. *et. al.*[9], Wang C. *et. al.*[10], Quan *et. al.*[11], Errea *et. al.*[12], Kruglov *et. al.*[13], Wang H. *et. al.*[14] and Duan *et. al.*[15, 16] on the same hydride based on BCS theory. The contradiction is clearly seen from the data. The present work focuses on the 250-kelvin lanthanum polyhydride, which has a positive dT_c/dp measured by Drozdov *et. al.* on $LaH_{9.6}$[1], and a negative dT_c/dp calculated by Errea *et. al.*[12] on *fcc*-LaH_{10} at pressures of 137-150 GPa.

Supplementary Figure 2

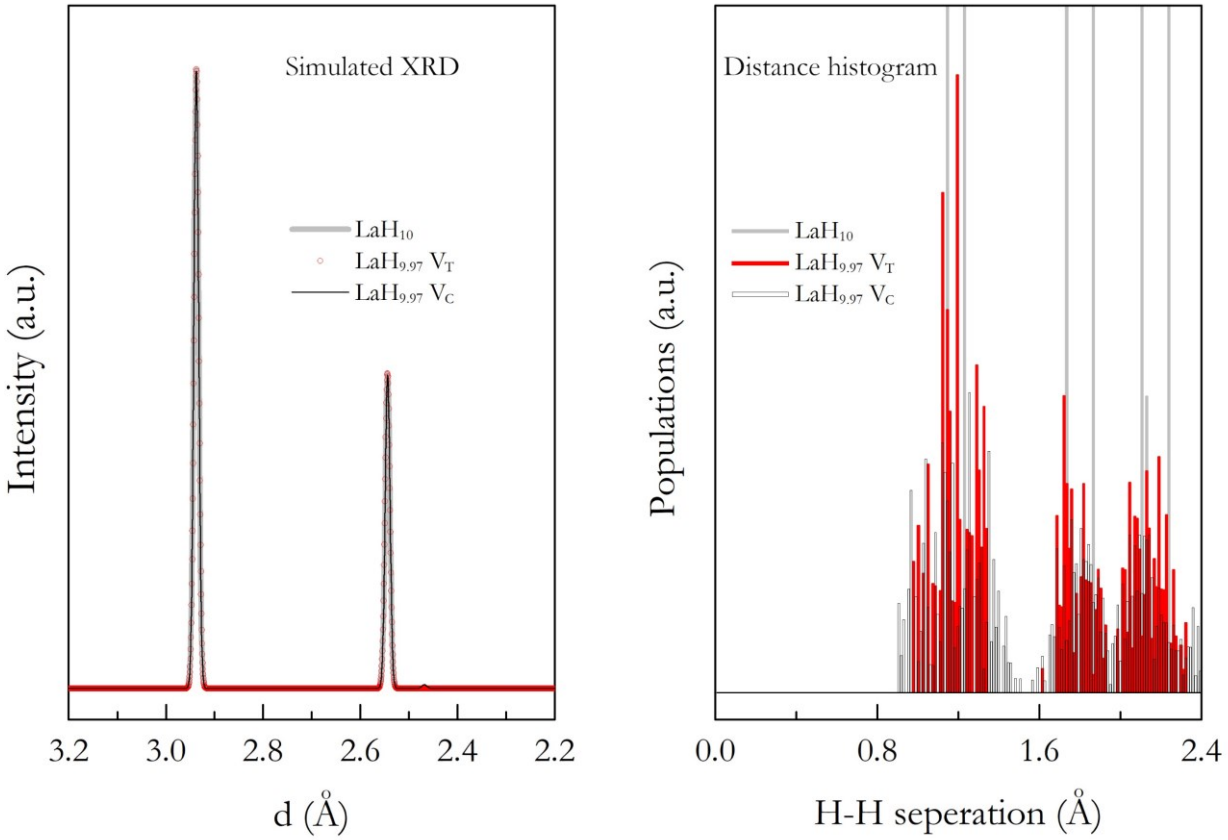

Supplementary Figure 2| Structural features of $LaH_{9.97}$ and *fcc*-LaH_{10} at 0 K.
The simulated XRD patterns of the static V_T and V_C structures of $LaH_{9.97}$ are almost identical to that of the *fcc*-LaH_{10} at 150 GPa, whereas the H-H separations in the V_T and V_C structures of $LaH_{9.97}$ distribute more broadly than that in *fcc*-LaH_{10}, indicating that the lattice distortion spreads out away from a vacancy site in the clathrate H framework of $LaH_{9.97}$. The 'a.u.' is the abbreviation of arbitrary unit, throughout the article.

Supplementary Figure 3

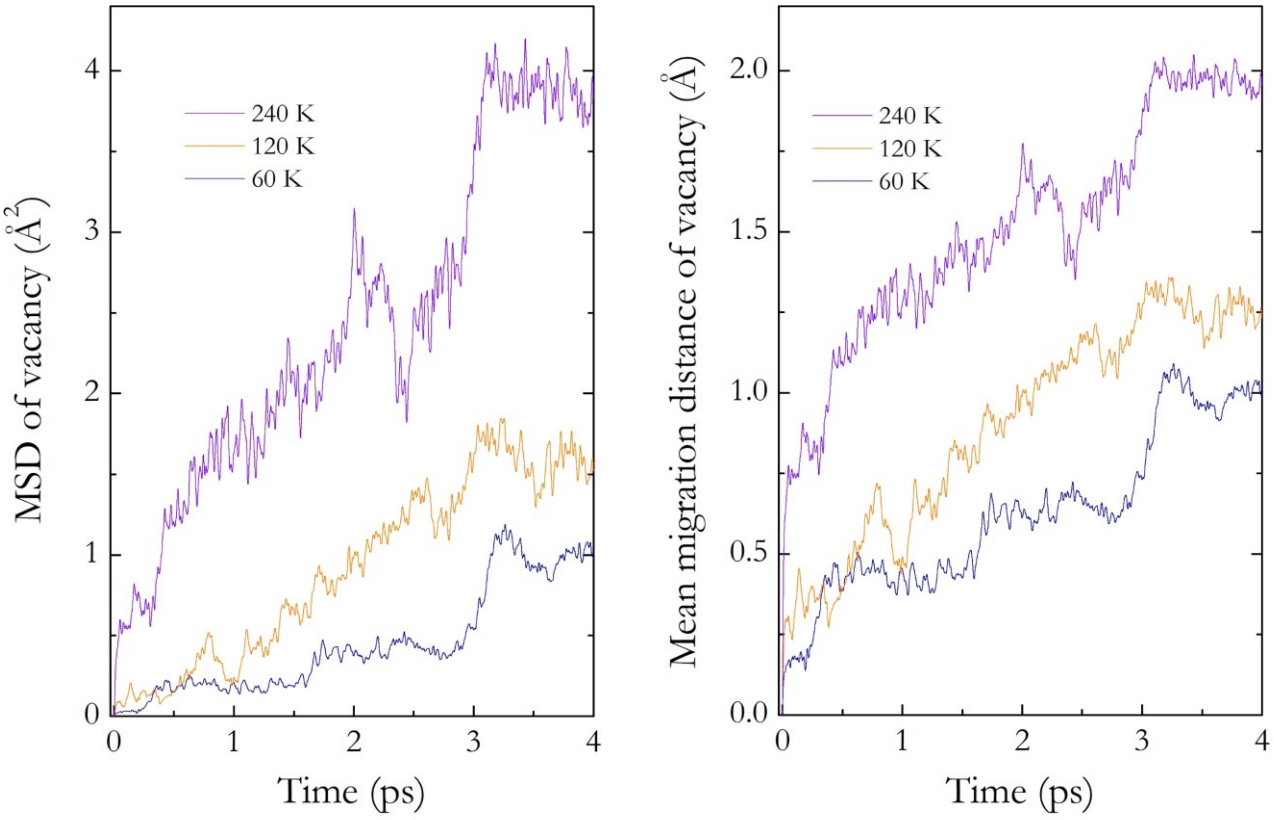

Supplementary Figure 3| Diffusion of vacancy in $LaH_{9.63}$ at 150 GPa.

The vacancy MSDs are derived from proton centroid trajectories in CMD simulations, which show at least one jump over a threshold value of 0.7 Å, the lower boundary of the first peak in the *g*(r), as shown in Supplementary Figure 4. The vacancy mean migration distance is defined as the square root of the MSD.

Supplementary Figure 4

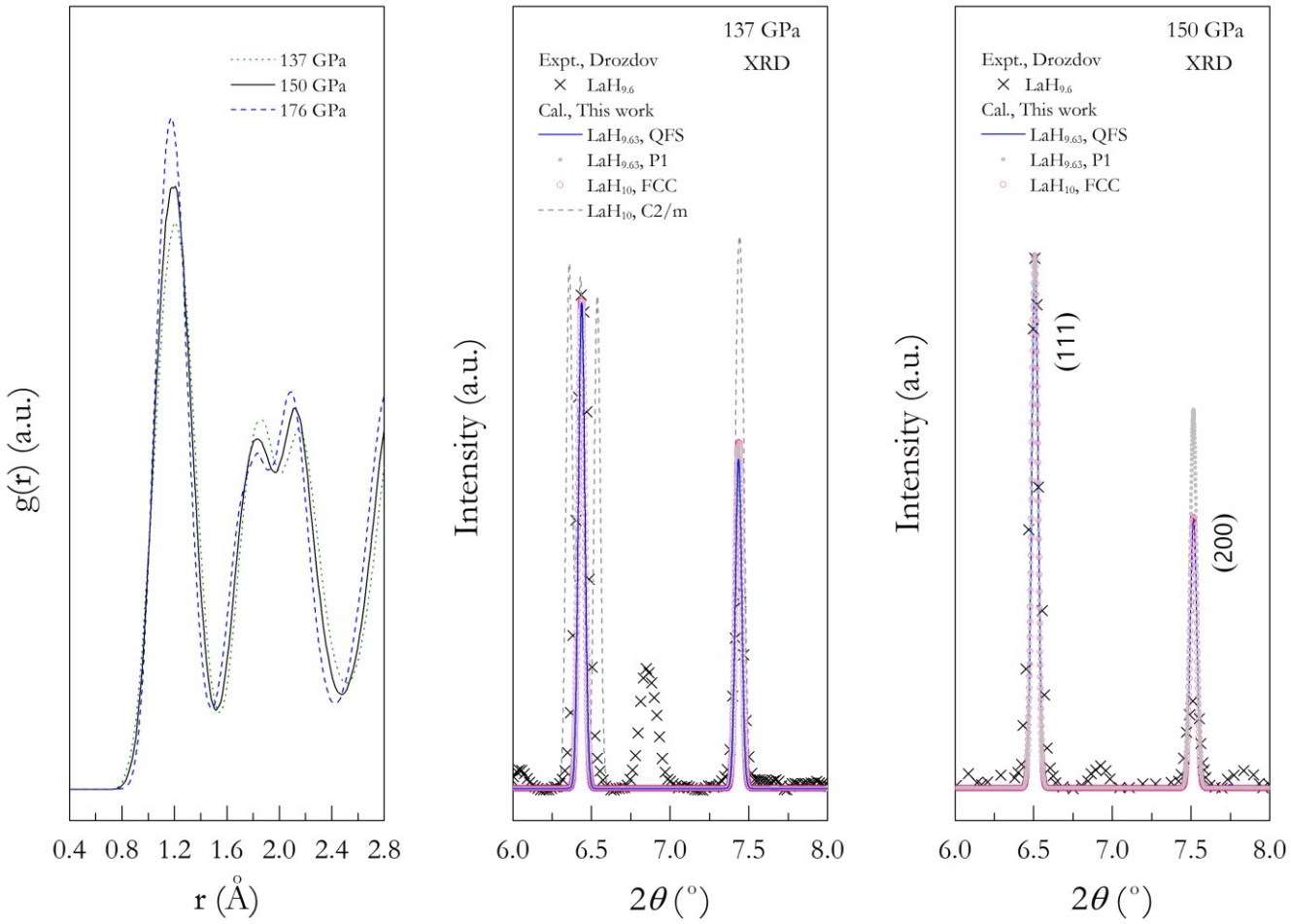

Supplementary Figure 4| Structural features of $LaH_{10-\delta}$.

The pairwise *g*(r) of H-H extracted from centroid trajectories of CMD simulations at 240 K between 137 and 176 GPa, and a comparison of the XRD pattern measured by Drozdov *et al.*[1] at 137 and 150 GPa to those calculated for the averaged La-substructure in $LaH_{9.63}$, and the static lattices of *P*1-$LaH_{9.63}$, *fcc*-LaH_{10} and *C*2/*m*-LaH_{10}.

Supplementary Figure 5

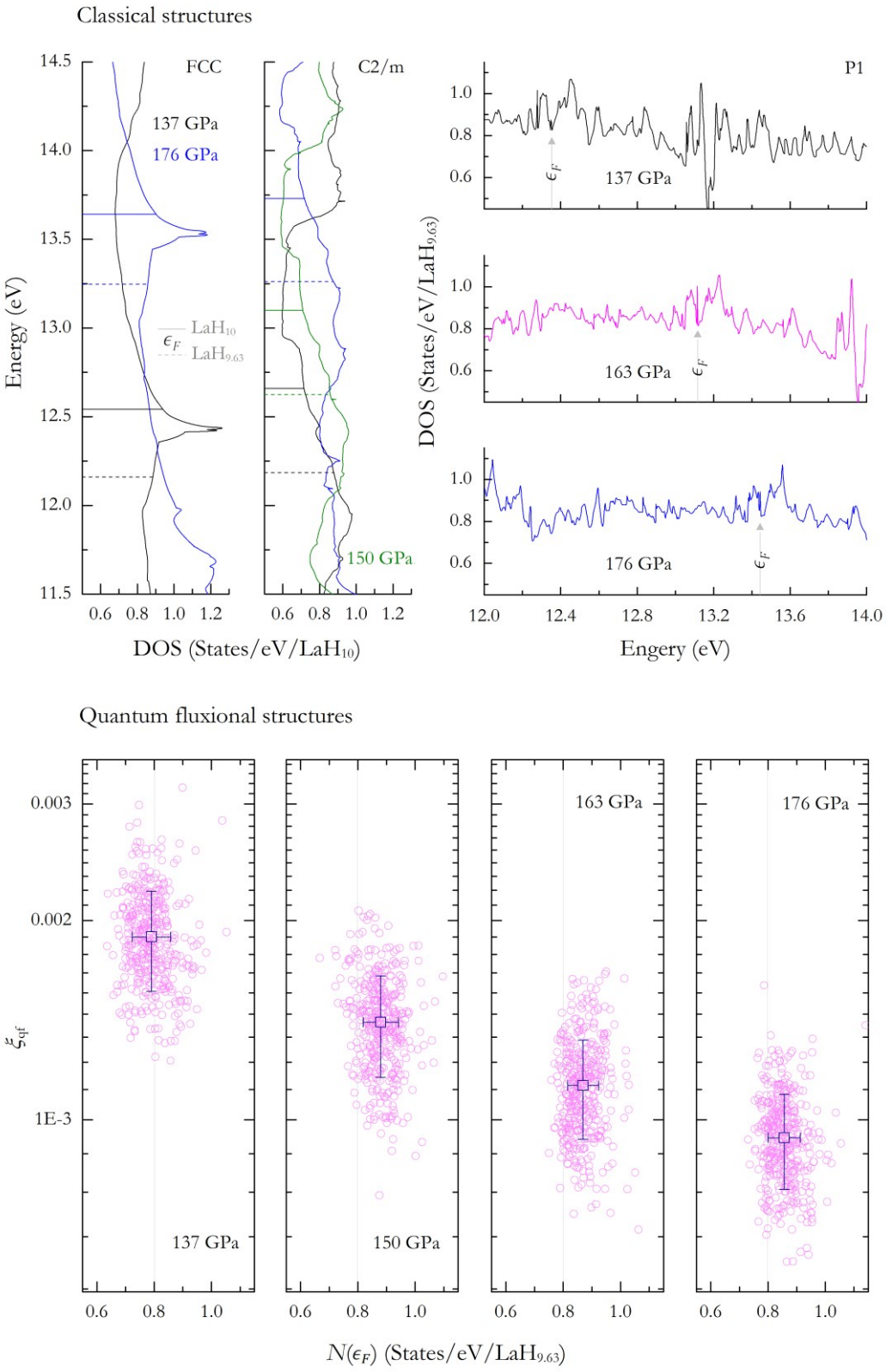

Supplementary Figure 5| Pressure effects on the electronic property of $LaH_{10-\delta}$.
The electron density of states (DOS) for static lattices of *fcc*-LaH_{10}, *C*2/*m* -LaH_{10} and *P*1-$LaH_{9.63}$, together with the distribution of $N(\epsilon_F)$ in quantum fluxional $LaH_{9.63}$ at 240 K against the configurational distance ξ_{qf} between 137 ~ 176 GPa, with error bar indicating the standard deviations. In the DOS of static *fcc*- and *C*2/*m* -LaH_{10}, the Fermi energy ϵ_F of $LaH_{9.63}$ obtained under the rigid-band approximation is also shown.

Supplementary Figure 6

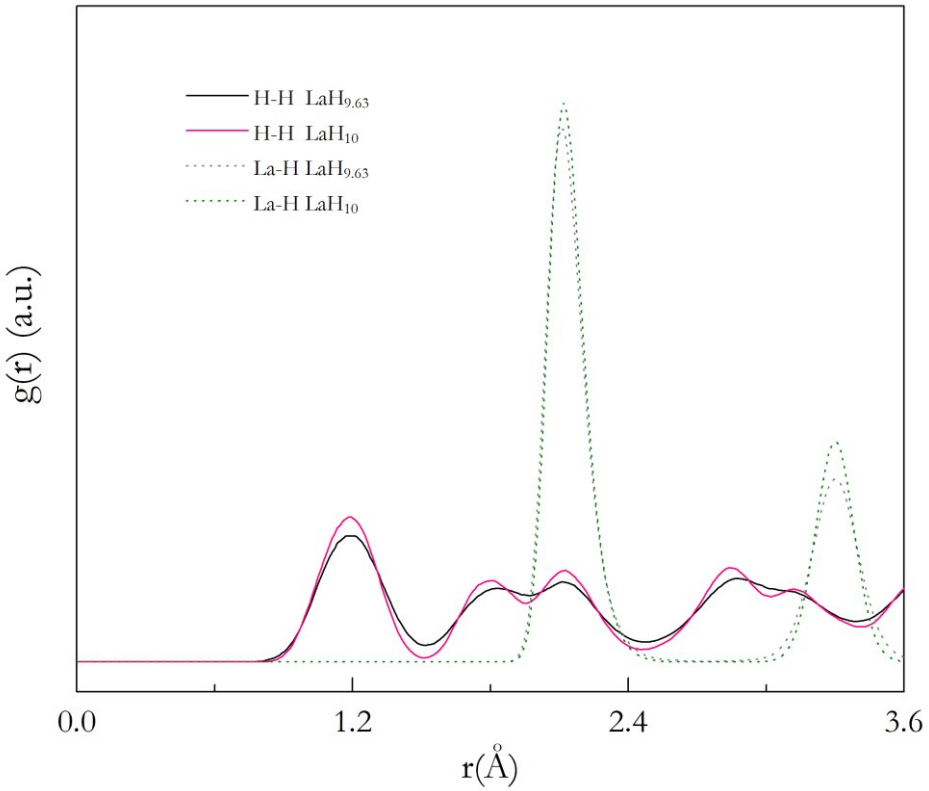

Supplementary Figure 6| Structural similarity between $LaH_{9.63}$ and LaH_{10}.
The pairwise *g*(r) of H-H and La-H extracted from centroid trajectories of CMD simulations at 240 K and 150 GPa for $LaH_{9.63}$ compared to those of *fcc*-LaH_{10}. The similarity in *g*(r) suggest that quantum fluxional $LaH_{9.63}$ largely retains the same local atomic environment as quantum *fcc*-LaH_{10}.

Supplementary Figure 7

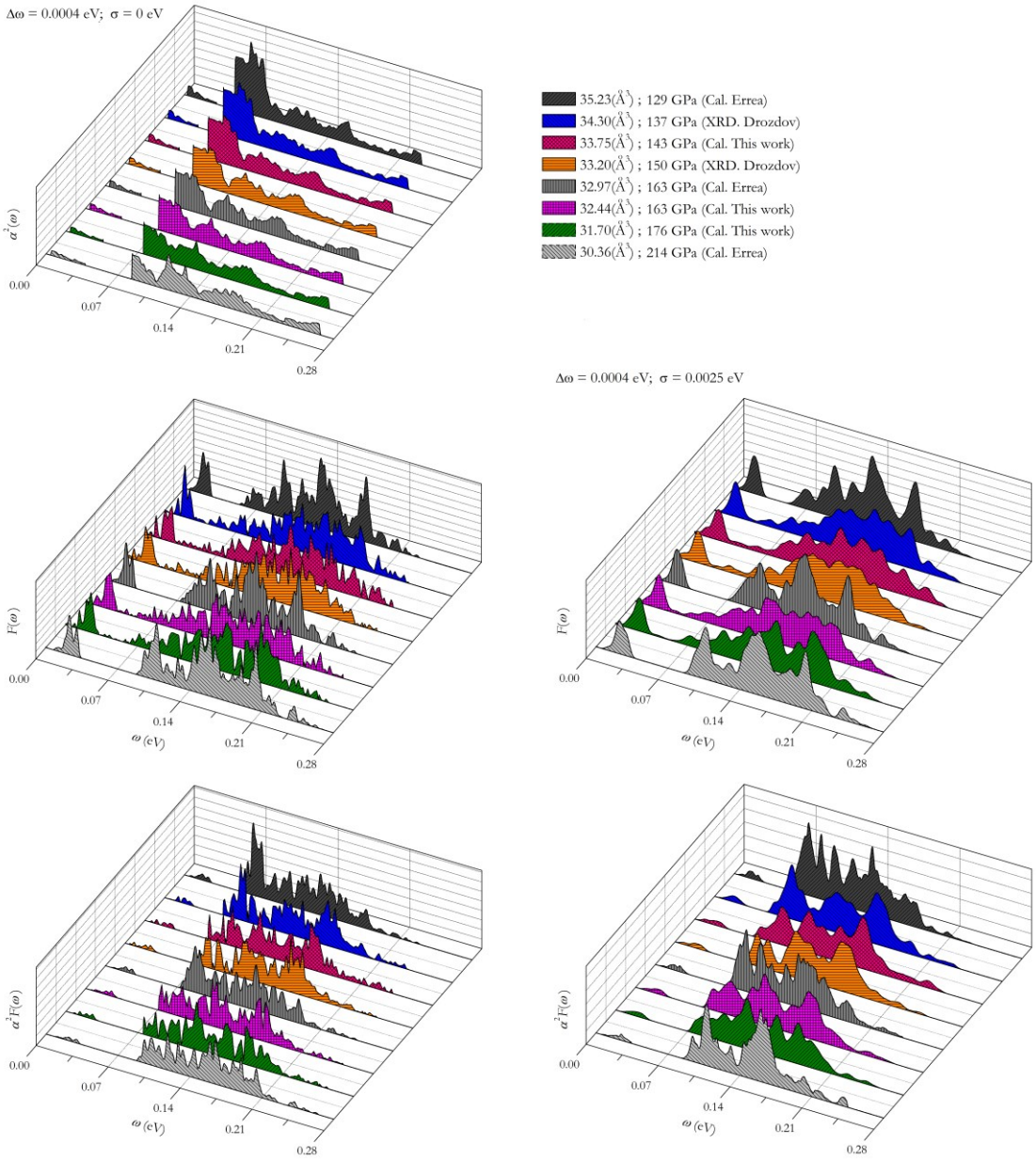

Supplementary Figure 7| The Eliashberg function in $LaH_{10-\delta}$.

The $d\Omega/dp$ (with Ω being ω_{log} or $\overline{\omega}_2$) for estimating the dT_c/dp in quantum fluxional $LaH_{9.63}$ is estimated based on the $F(\omega)$ of $LaH_{9.63}$ obtained by Fourier transforming the velocity autocorrelation functions in the CMD simulations at 240 K in combination with coupling functions $\alpha(\omega)^2$ approximated by that of quantum *fcc*-LaH_{10}[12]. The $\alpha(\omega)^2$ at 129, 163 and 214 GPa are derived from $\alpha(\omega)^2F(\omega)$ and $F(\omega)$ of Ref. 12. The $\alpha(\omega)^2$ at other pressures within 137 ~ 176 GPa are calculated by inverse volume weight interpolation of neighboring coupling functions. With increasing of pressure, $LaH_{9.63}$ exhibits slight phonon hardening in $F(\omega)$, similar to quantum *fcc*-LaH_{10}. Compared to the $F(\omega)$ of quantum *fcc*-LaH_{10}, those of $LaH_{9.63}$ spread a bit wider, which is attributed to temperature effects: The former and the latter are derived at 0 and 240 K, respectively. Smeared $F(\omega)$ is generally adopted to converge EPC parameters, and we smear the $F(\omega)$ by a Gaussian profile with widths (σ) of 0.002 ~ 0.003 eV in this work. The original spectrum and those with σ of 0.0025 eV are shown here. The pressure-volume relations measured by Drozdov *et al.*[1], calculated by Errea *et al.*[12] and estimated in this work are shown in the labels.

Supplementary Table 1

Hydrides	P (GPa)	ΔP (GPa)	T_c (K)	$\Delta T_c/\Delta P$ (K/GPa)	ω_{log} (meV)	$\Delta\omega_{log}/\Delta P$ (meV/GPa; %)	λ	$\Delta\lambda/\Delta P$ (GPa^{-1}; %)	ζ (1/eV^2)	$\Delta\zeta/\Delta P$ (1/eV^2/GPa; %)	β (eV^2)	$\Delta\beta/\Delta P$ (eV^2/Megabar; %)
Theoretical analysis of literature data												
LaH_{10} (Ref. 12)	129 ~ 214	85	252.6 ~ 235.9	**-0.196**	76.4 ~ 115.5	**+0.460; +51**	3.62 ~ 2.06	**-0.0184; -43**	93.5 ~ 43.8	**-0.585; -53**	0.039 ~ 0.047	**+0.00941; +21**
LaH_{10} (Ref. 8)	210 ~ 300	90	246.0 ~ 223.0	**-0.256**	72.5 ~ 123.2	**+0.563; +70**	3.62 ~ 1.81	**-0.0201; -50**	83.1 ~ 36.1	**-0.522; -57**	0.044 ~ 0.050	**+0.00667; +14**
LaH_{10} (Ref. 10)	220 ~ 300	80	234.2 ~ 215.7	**-0.231**	57.9 ~ 115.6	**+0.722; +100**	4.24 ~ 1.86	**-0.0298; -106**	100.1 ~ 40.1	**-0.750; -60**	0.042 ~ 0.046	**+0.00500; +10**
LaH_{10} (Ref. 11)	250 ~ 300	50	206 ~ 189	**-0.340**	92 ~ 115	**+0.460; +25**	2.46 ~ 1.80	**-0.0132; -27**	59.1 ~ 40.9	**-0.364; -31**	0.042 ~ 0.044	**+0.00400; +5**
CaH_6 (Ref. 14)	150 ~ 250	100	221.6 ~ 190.8	**-0.308**	88.8 ~ 118.0	**+0.292; +33**	2.66 ~ 1.63	**-0.0103; -39**	31.9 ~ 17.1	**-0.148; -46**	0.083 ~ 0.095	**+0.01200; +14**
CaH_6 (Ref. 11)	150 ~ 250	100	200 ~ 180	**-0.200**	90 ~ 117	**+0.270; +30**	2.53 ~ 1.69	**-0.0084; -33**	30.8 ~16.9	**-0.139; -45**	0.082 ~ 0.100	**+0.01800; +21**
This work												
$LaH_{9.63}$	137 ~ 163	26	209.88 ~ 228.09	**+0.700**	84.20 ~ 94.40	**+0.392; +12**	2.535 ~ 2.452	**-0.0032; -3**	62.887 ~ 56.337	**-0.252; -10**	0.04031 ~ 0.04352	**+0.01235; +8**
	163~ 176	13	228.09 ~ 222.02	**-0.467**	94.40 ~ 99.42	**+0.386; +5**	2.452 ~ 2.240	**-0.0163; -9**	56.337 ~ 50.036	**-0.485; -11**	0.04352 ~ 0.04476	**+0.00954; +3**
	Stability of the +$\Delta T_c/\Delta P$ slop against variation of β (± 50%)											
	137 ~ 163	26	103.06 ~ 110.51	+0.287	84.20 ~ 94.40	**+0.392; +12**	1.267 ~ 1.226	-0.0016; -3	62.887 ~ 56.337	**-0.252; -10**	0.02015 ~ 0.02176	**+0.01235; +8**
	137 ~ 163	26	290.04 ~ 315.56	+0.982	84.20 ~ 94.40	**+0.392; +12**	3.802 ~ 3.678	-0.0048; -3	62.887 ~ 56.337	**-0.252; -10**	0.06046 ~ 0.06528	**+0.01235; +8**
	Limit of stability of the +$\Delta T_c/\Delta P$ slop against $\Delta\beta/\Delta P$ slop											
	137 ~ 163	26	228.09 ~ 228.09	-0.00	84.20 ~ 94.40	**+0.392; +12**	2.801 ~ 2.452	-0.0134; -12	62.887 ~ 56.337	**-0.252; -10**	0.04454 ~0.04352	-0.00392; -3

Supplementary Table 1| Parameters impacting the pressure trend of T_c.

Based on retrievable $\Omega(p)$ (where Ω represents ω_{log} or $\bar{\omega}_2$) (Ref 11) or $\alpha(\omega)^2F(\omega)$ from the literature (Ref 12, 8, 10 and 14), we derived $d\Omega/dp$ and analyzed the role played by several parameters in the pressure trend of T_c using AD equations, with the Coulomb coupling constant μ^* set to 0.1. The resulting pressure trends of T_c for cubic LaH_{10} and CaH_6 are in good agreement with the literature (Supplementary Figure 1). The analysis demonstrates that ζ decreases more than two times faster than β increases upon compression, which leads to a negative sign of the $d\lambda/dp$ slope. This suggests that $d\zeta/dp$ dominates the pressure trend of λ. λ has a monotonously negative pressure dependence, but decreases less significantly than ω_{log} increases. However, due to the nonlinear dependence of T_c on λ, either through the well-known exponential function or the 'strong-coupling correction' and 'shape correction' factors (see details in page 14), $d\lambda/dp$ plays a dominant role in determining the dT_c/dp slope.

Our results for $LaH_{9.63}$ are also shown in order to enable a direct comparison. Our $d\omega_{log}/dp$ is comparable to those of cubic LaH_{10} (*fcc*) and CaH_6 (*bcc*), but $d\zeta/dp$ decreases significantly at lower pressures, which reverses the sign of the dT_c/dp slope through a considerable reduction of $d\lambda/dp$ below 163 GPa. We further estimated the limit of stability of the $+dT_c/dp$ slope against variations of β and $d\beta/dp$: I) at a fixed $d\beta/dp$ of 0.01235 eV^3/megabar, decreasing (increasing) β by 50 % results in a decrease (an increase) of dT_c/dp by 59% (41%), but does not change the positive sign; II) at a fixed β of 0.04352 eV^3 at 176 GPa, an about 127 % decrease of the $d\beta/dp$ slope is needed to invert the sign of dT_c/dp. Literature data generally report a positive $d\beta/dp$ slope for cubic hydrides covering a range of H/M ratios (M= La and Ca) from 10 to 6. Therefore, $LaH_{9.63}$ is very unlikely to exhibit a $-d\beta/dp$ slop in qualitative contradiction with most other hydrides. The analysis indicates that the $+dT_c/dp$ slope is robust to errors induced by the approximation of β and $d\beta/dp$ in $LaH_{9.63}$ by those in quantum *fcc*-LaH_{10}.

Supplementary Table 2

Pressure (GPa)	$N(\epsilon_F)$ (1/eV²)	ω_{log} (meV)	$\bar{\omega}_2$ (meV)	ζ (1/eV³)	β (eV³)	λ	T_c (K)
σ =0 for $\alpha(\omega)^2$; σ =0.0025 eV for $F(\omega)$; $\Delta\omega$ = 0.0004 eV							
137	0.79	84.20	112.11	62.887	0.04031	2.535	209.88
143	0.855	84.70	118.26	61.121	0.04128	2.523	212.42
150	0.880	88.24	123.06	58.088	0.04224	2.454	215.94
163	0.869	94.40	124.20	56.337	0.04352	2.452	228.09
176	0.856	99.42	130.82	50.036	0.04476	2.240	222.02
σ = 0.01 & 0.05 eV for $\alpha(\omega)^2$; σ =0.0025 eV for $F(\omega)$; $\Delta\omega$ = 0.0004 eV							
137	0.790	84.16 & 63.11	112.30 & 106.98	62.684 & 69.06	0.04031	2.527 & 2.783	209.30 & 178.21
163	0.869	95.69 & 80.10	124.83 & 121.62	55.769 & 58.75	0.04352	2.427 & 2.557	228.79 & 206.31
176	0.856	100.81 & 88.75	131.68 & 130.54	49.381 & 50.25	0.04476	2.210 & 2.249	222.20 & 202.66
Reshaping $\alpha^2F(\omega)$ by artificial scaling of $\Delta\omega$ to 0.0003 & 0.0005 eV; σ =0 for $\alpha(\omega)^2$; σ = 0.0025 eV for $F(\omega)$							
137	0.790	61.89 & 106.33	83.67 & 140.50	112.900 & 40.042	0.04031	4.551 & 1.614	245.34 & 172.95
163	0.869	69.91 & 119.01	92.90 & 155.53	100.696 & 35.924	0.04352	4.382 & 1.563	267.35 & 186.79
176	0.856	73.56 & 125.12	97.81 & 163.78	89.500 & 31.923	0.04476	4.006 & 1.429	263.36 & 177.40

Supplementary Table 2| Parameters for estimating the pressure trend of T_c.

Parameters for calculating the pressure trend of T_c shown in Fig 4b with smearing σ = 0.0025 eV for $F(\omega)$ are listed here for illustration. Furthermore, we compare the pressure trends of T_c calculated for various σ of $\alpha(\omega)^2$ (*i.e.* 0, 0.01 and 0.05). It is found that the trend is determined by the overall shape of $\alpha(\omega)^2$. Due to the inexistence of a method that can directly calculate the $\alpha^2F(\omega)$ of a quantum fluxional structure, we estimated frequency moments Ω of $\alpha^2F(\omega)$ in $LaH_{9.63}$ based on the calculated $F(\omega)$ of $LaH_{9.63}$ and the $\alpha(\omega)^2$ approximated by that of quantum *fcc*-LaH_{10}[12]. To evaluate the potential errors associated with the approximation, we calculated the T_c using reshaped $\alpha^2F(\omega)$ obtained by artificial scaling of $\Delta\omega$. Empirically, EPC weights the phonon spectrum to lower frequencies in high-T_c hydrides. This weighting effect changes smoothly with pressure, as observed from the shape of $\alpha(\omega)^2$ in quantum *fcc*-LaH_{10} (Supplementary Figure 7). Considering this, and that quantum $LaH_{9.63}$ and *fcc*-LaH_{10} exhibit a similar phonon hardening trend with increasing pressure as well as similar shapes of $F(\omega)$, our results suggest that the pressure trend of T_c is robust to variations of Ω. This indicates that it is practicable to estimate qualitatively the sign of dT_c/dp slop in $LaH_{9.63}$ under this approximation.

Computational Details

Molecular dynamics calculations

Quantum nuclear dynamics were studied using path-integral molecular dynamics (PIMD) and centroid molecular dynamics (CMD), with the massive Nosé-Hoover chain (NHC) thermostats on NVT and NVE ensembles (N-number of particles; V-volume; T-temperature, and E-energy), respectively, as implemented in the PIMD code[17]. NpT-PIMD (p-pressure) simulations were performed to estimate the quantum pressure-volume relations. Beads number was set to 16 for the cases without a specification, and time step was set to 0.5 and 0.05 fs for PIMD and CMD, respectively. A short PIMD simulation was always carried out on the initial structure to prepare the pre-equilibrium state in order to promote the efficiency and stability of the CMD simulation. The parameters of the standard *ab initio* MD simulations are the same as those of the PIMD simulations, except for a reduced bead number of 1. The MD runs of $LaH_{9.63}$ were initialized from different centroid configurations of the 4-picosecond CMD trajectory with a sampling interval of 0.25 ps for 16 short runs of 12000 steps and of 1 ps for 4 long runs of 52000 steps.

The underlying *ab initio* total energy and forces were calculated based on the plane-wave pseudopotential method, as implemented in the Vienna *ab initio* simulation program (VASP)[18]. The convergence criterion for the total energy (Ecc) was chosen to be 3×10^{-6} eV/atom with a plane-wave cutoff of 325 eV and Γ-point sampling of the first Brillouin zone. Decreasing Ecc to 3×10^{-7} eV/atom (run 2) results in a nearly negligible change of the proton diffusion coefficient D in $LaH_{9.63}$ at 150 GPa (see Fig. 3a in the main text). The volume of the cubic simulation cells of $LaH_{9.63}$ were fixed at 1097.70, 1079.98, 1062.39, 1038.16, and 1014.35 $Å^3$. The resulting temperature fluctuations at equilibrium are within ± 15 K, ± 10 K and ± 25 K with respect to the target in the PIMD, CMD and MD simulations, respectively. Other details are summarized in Supplementary Table 3.

Supplementary Table 3. Details of simulations.

Phase	Number of Atoms, H : La	Pressures, GPa	Temperature, K	Method	Steps	runs
$LaH_{9.63}$	308:32	150	60, 120, 240	MD	12000	1-16
		137, 143, 150, 163,176	240	MD	52000	1-4
		150	240	PIMD	2000	1,2
				CMD	82000	1,2
		137, 143, 163,176	240	PIMD	2000	1
				CMD	82000	1
		150	60	PIMD	8000	3§
			60, 120	PIMD	2000	1
				CMD	82000	1
$LaH_{9.0}$	288:32	130, 137, 150, 170, 180	300	PIMD†	2000	1
LaH_{10}	320:32	130, 137, 150, 170, 180	300	PIMD†	2000	1
		137, 150	240	PIMD	2000	1
				CMD	42000	1

§NVT simulations with 16, 32 and 64 beads were performed to check the impact of bead number on MSD; †NpT simulations.

The quantum pressure-volume relation of *fcc*-LaH_{10} and *fcc*-LaH_9.

The quantum pressure-volume relation of *fcc*-LaH_{10} and *fcc*-LaH_9 at 300 K was estimated from the volume averaged over 1 ps at equilibrium obtained in NpT-PIMD simulations using a cubic box and Martyna's equation of motion, as implemented in the PIMD code[17]. Our results reveal a H/La ratio of 9.54 (or 9.71) for the experimental samples synthesized at 150 GPa (or 137 GPa), in good agreement with experimental estimation of a $LaH_{9.6}$[1]. To ensure our pressure trend of T_c can directly compare with the experimental one, we built structural models at 137 and 150 GPa using experimental lattice parameters. This guarantees that the coincidence of this pressure range (*i.e.* '137-150 GPa') between calculation and experiments does not dependent on the experimental or theoretical pressure scales. Notably, this is indeed the pressure range that the positive dT_c/dp slope were measured experimentally and calculated in this work. The PBE functionals may lead to potential shift of the calculated T_c *v.s.* pressure curve in relative to the experimental measured one at pressure above 150 GPa, however, which does not affect our conclusion. The quantum pressure of 143, 163 and 176 GPa were estimated based on interpolation.

The mean square displacement, $\langle \Delta \boldsymbol{r^2} \rangle$

$$\langle \Delta r(t)^2 \rangle = \langle |r_i(t) - r_0(t) - [r_{cm}(t) - r_{cm}(0)]|^2 \rangle_I,$$

where $r_i(t)$ is the position of the diffusive proton *i*, which exhibits at least one jump over a threshold value of 0.7 Å over the course of the simulation, $r_{cm}(t)$ represents the position of the center of mass of the system at the time *t*, and the $\langle\ \rangle$ represent an average over 10 time steps and the total number of 'particle' *I*, which equals 308 for proton and 12 for vacancy in $LaH_{9.63}$. In the simulations, some of diffusive protons hop back to the previously occupied position occasionally due to 'traffic jam', which results in a decrease of $\langle \Delta \boldsymbol{r^2} \rangle$. The proton traffic jam and local structural relaxation result in plateaus in $\langle \Delta \boldsymbol{r^2} \rangle$ curves in both the CMD and MD simulations. However, $\langle \Delta \boldsymbol{r^2} \rangle$ generally increases with increasing of t, which is clearly revealed by long-time MD simulations of 24 ps.

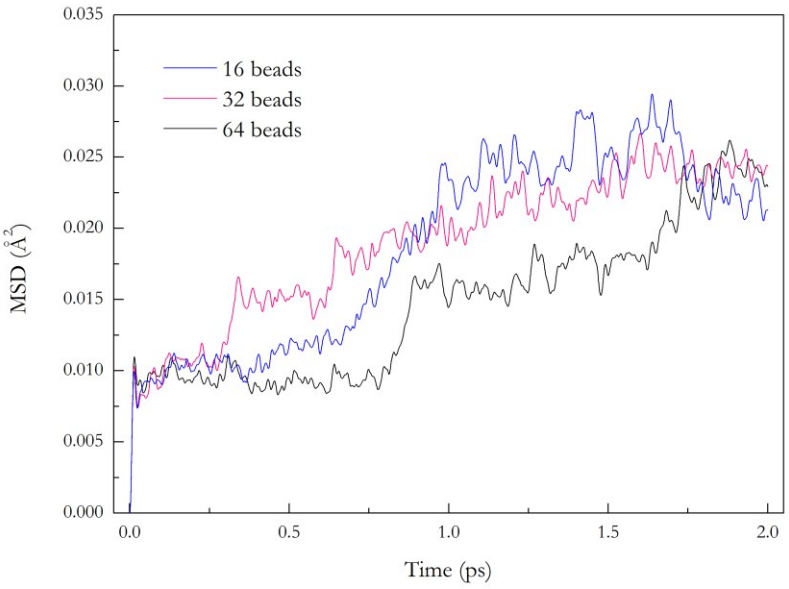

Supplementary Figure 8. MSD of PIMD simulation with various bead numbers at 60 K.

MSDs derived from the centroid trajectory of PIMD simulations at 150 GPa and an equilibrium temperature of 60 K with 16, 32 and 64 beads are shown in Supplementary Figure 8. All curves suggest quantum proton diffusion at this temperature. Considering that the strength of NQE increases with decreasing temperature, larger bead number gives better MSD. The difference of $\langle \Delta \boldsymbol{r^2} \rangle$ values at the end of the simulation (*i.e.* 2 ps) is not significant, which may be attributed to the 'traffic jam' of protons in $LaH_{9.63}$ associated with the small amount of stoichiometric defect.

The diffusion coefficient, *D*

We approximate the proton diffusion coefficient D in $LaH_{9.63}$ from the slope of $\langle \Delta r^2 \rangle$ obtained from a linear fit, as shown in Supplementary Figure 9 for CMD simulations run1 and run2 at 150 GPa and 240 K. D is computed from $D = slope(\langle \Delta r^2 \rangle)/6$.

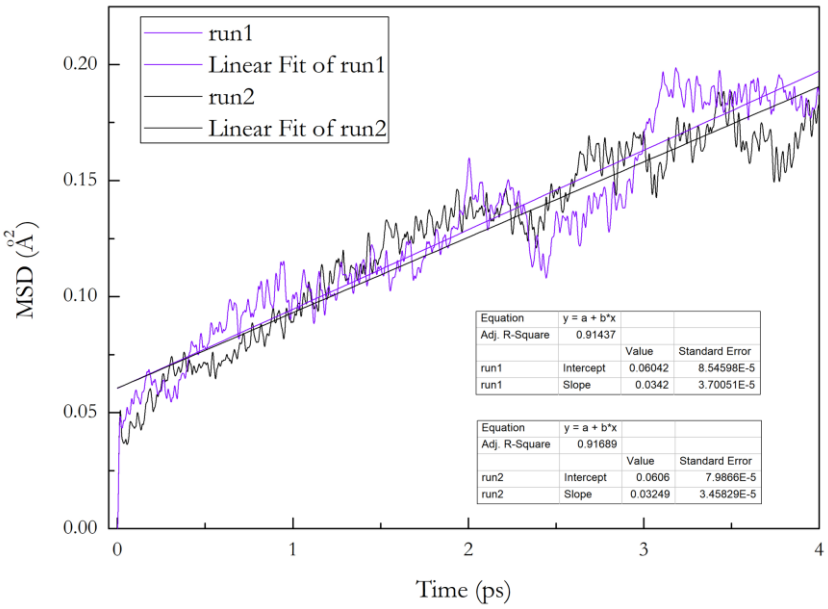

Supplementary Figure 9. Linear fit of MSD.

Vacancy formation enthalpy, H^f

We carried out a full variable-cell optimization (using ISIF=3 in VASP) of *fcc*-LaH_{10}[7, 8] (in a 2×2×2 supercell of the conventional unit cell containing 352 atoms) and *B*2/*n*-H_2 (in the conventional unit cell of 48 atoms)[19] at pressures between 120 and 220 GPa with an interval of 5 GPa. We employed *k*-mesh grids of sizes 3×3×3 and 15×9×9, respectively, to carry out the required DFT calculations.

The V_T and V_C $LaH_{9.97}$ vacancy structures were then constructed by removing the appropriate H atom from the relaxed *fcc*-LaH_{10} structure at each pressure, as described in the main text. Variable-cell optimization of these structures induced proton diffusion, resulting in a distortion of the structures. In order to isolate the effect of the vacancies, therefore, we only relaxed the atomic positions, keeping the cell shape and volume fixed (ISIF=2 in VASP). We used a *k*-mesh grid equivalent to that for *fcc*-LaH_{10}. A cut-off energy of 325 eV and a convergence criterion for the total energy of 3×10^{-7} eV/atom were employed in all calculations.

Using the resulting *V-E* relationship of the relaxed structures, the pressure-enthalpy curves were then calculated using the third-order Birch–Murnaghan isothermal equation of state[20]. From the enthalpies for each pressure, the H^f of the V_C and V_T structures were calculated as follows,

$$H^f = H(LaH_{9.97}) - H(fcc\text{-}LaH_{10}) + H(B2/n\text{-}H_2)/48,$$

with the configurationally averaged H^f expressed as,

$$H^f(\text{average}) = 0.2\times H^f(V_T) + 0.8\times H^f(V_C).$$

The calculated pressure-volume curve gives a pressure shift of ~5 GPa for $LaH_{9.97}$ with respect to the experimental measurements on *fcc*-$LaH_{9.6}$ at 120-220 GPa, which does not affect our discussions.

It should be noted that H^f is calculated classically in the static lattice approximation on the Born–Oppenheimer energy surface, which differs from the configurational energy surface of the quantum crystal (e.g., *fcc*-LaH_{10} in Ref. 12) or the free energy surface of the classical or quantum crystal at finite temperature. The stability and pressure boundary of the

vacancy structure may be affected by more complex physical effects existing in the superconducting samples, for instance nuclear quantum effects (including zero-point motion of nuclei and proton tunnelling), or temperature effects. Indeed, temperature effects only enhance the formation of vacancies. In this sense, the conclusion from the H^f curves shown in Fig.1a of the main text, namely that vacancy formation is favored below 158 GPa in the classical crystal picture, while being based on a model calculation subject to many approximations, indicates that lanthanum superhydride should be rather prone to vacancy formation.

The configurational distance, ξ

The crystal fingerprint technique utilized in this study is based on Gaussian overlap matrices, which represent the local environments of all atoms in a unit cell and can efficiently determine configurational distances ξ between crystalline structures satisfying the mathematical requirements of a metric[21]. The ξ of the QFS of $LaH_{9.63}$ *vs.* various static structures (e.g. *fcc*, *C*2/*m* and *P*1) were obtained by statistical analysis over the ξ of 400 centroid configurations sampled from 16-bead CMD trajectories of 4 ps with a time interval of 10 fs at each pressure.

Electronic density of states at the Fermi level, $N(\epsilon_F)$

The $N(\epsilon_F)$ is of central importance to the understanding of conventional superconductivity for hydrogen-rich materials. It is quite general that the pressure dependence of $N(\epsilon_F)$ directly correlates to the pressure trend of the superconducting T_c. The $N(\epsilon_F)$ of the quantum structures of $LaH_{9.63}$ was calculated by carrying out a statistical average over the $N(\epsilon_F)$ of 400 centroid configurations sampled from 16-bead CMD trajectories of 4 ps with a time interval of 10 fs at each pressure. The $N(\epsilon_F)$ of each centroid configuration was calculated using the tetrahedron method with Blöchl corrections[22], with a convergence criterion for the total energy of 3×10^{-6} eV/atom for a cut-off energy of 325 eV and a 5×5×5 *k*-mesh grid. The $N(\epsilon_F)$ of static *fcc*-LaH_{10}, *C*2/*m*-LaH_{10}, and *P*1-LaH_{10} were calculated based on primitive cells by the tetrahedron method with Blöchl corrections, with a convergence criterion for the total energy of 3×10^{-6} eV/atom for a cut-off energy of 325 eV and 21×21×21, 27×27×15 and 5×5×5 *k*-mesh grids, respectively. For the *fcc* and *C*2/*m* phases, the $N(\epsilon_F)$ of static $LaH_{9.63}$ were estimated based on the rigid-band model[23] of the electronic structure of LaH_{10} by virtue of an artificial shift of ϵ_F.

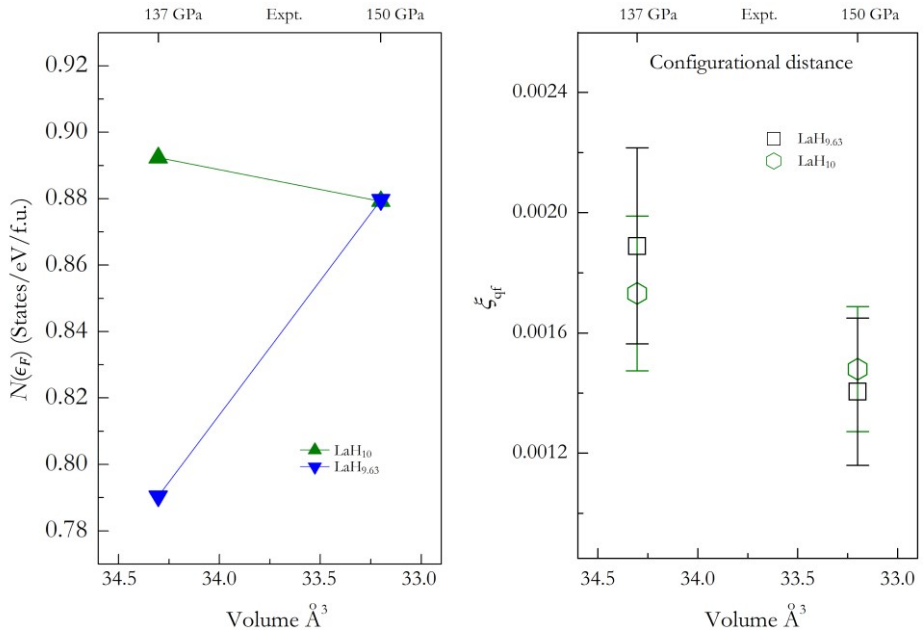

Supplementary Figure 10. The $N(\epsilon_F)$ and ξ (of H substructure) in $LaH_{9.63}$ compared to those of LaH_{10}. The f.u. is the abbreviation of formula unit, throughout the article.

Comparison on $N(\epsilon_F)$ and ξ between $LaH_{9.6}$ and LaH_{10}

As shown in Supplementary Figure 10, we compared the configurationally averaged ξ and $N(\epsilon_F)$ in quantum $LaH_{9.63}$ and LaH_{10} in the pressure range of 137–150 GPa. The results suggest that the H sublattice distortion is suppressed in the vacancy-free case. Moreover, a negative $dN(\epsilon_F)/dp$ slop is observed in LaH_{10}, in contrast to the positive $dN(\epsilon_F)/dp$ slop of $LaH_{9.63}$.

The frequency moments of $\alpha^2F(\omega)$ in $LaH_{9.63}$, ω_{log} and $\bar{\omega}_2$

The $\alpha^2F(\omega)$ of $LaH_{9.63}$ is estimated based on the $F(\omega)$ of $LaH_{9.63}$ derived by Fourier transforming the velocity autocorrelation functions (VACF) in the CMD simulations at 240 K in combination with coupling functions $\alpha(\omega)^2$ approximated by that of quantum *fcc*-LaH_{10}:

1. Deriving the $F(\omega)$ of $LaH_{9.63}$ by Fourier transforming the VACF in the CMD simulations at 240 K and volume (V) of 34.30, 33.75, 33.20, 32.44, and 31.70 Å^3/f.u.;
2. Calculating the $\alpha(\omega)^2$ from $\alpha^2F(\omega)$ and $F(\omega)$ in quantum *fcc*-LaH_{10}: $\alpha(\omega)^2 = \alpha^2F(\omega)/F(\omega)$ at volume (V') of 35.23, 32.97 and 30.36 Å^3/f.u., and deriving the $\alpha(\omega)^2$ at V by inverse volume weight interpolation of $\alpha(\omega)^2$ of neighboring V';
3. Calculating the $\alpha(\omega)^2F(\omega)$ of $LaH_{9.63}$ based on $F(\omega)$ of $LaH_{9.63}$ and $\alpha(\omega)^2$ of quantum *fcc*-LaH_{10}: $\alpha^2F(\omega)_{\_LaH9.63} = \alpha(\omega)^2_{\_LaH10} \times F(\omega)_{\_LaH9.63}$ at various V values;
4. Calculating the ω_{log} and $\bar{\omega}_2$ following their definitions in Ref. 24.

The frequency step $\Delta\omega$ is set to 0.0004 eV in the calculations. To include the vibrational modes in both of low- and high-frequency regime, the $F(\omega)$ are derived from the VACFs of the La and H sublattices separately. Since smeared $F(\omega)$ is generally adopted to converge EPC parameters, we smear $F(\omega)$ with Gaussian profiles with widths (σ) of 0.002 ~ 0.003 eV. ω_{log} and $\bar{\omega}_2$ are therefore obtained following their definitions in Ref. 24. In addition, we reshaped the $\alpha^2F(\omega)$ of $LaH_{9.63}$ by artificial scaling of $\Delta\omega$ to 0.0003 and 0.0005 eV to evaluate the potential errors associated with the approximation in step 3, see the caption of Supplementary Table 2.

The electron-phonon coupling constant, λ

We estimate λ in $LaH_{9.63}$ using McMillan's formula[25] ($\lambda = N(\epsilon_F)\langle I^2\rangle/M\bar{\omega}_2^2$) as follows:

1. Combining variables as $\lambda = \beta \cdot \zeta$ with $\beta = \langle I^2\rangle/M$ and $\zeta = N(\epsilon_F)/\bar{\omega}_2^2$;
2. Estimating $\zeta(V)$ based on $N(\epsilon_F)$ and $\bar{\omega}_2$ of $LaH_{9.63}$ at V of 34.30, 33.75, 33.20, 32.44, and 31.70 Å^3/f.u.;
3. Calculating $\beta(V')$ from λ, $N(\epsilon_F)$ and $\bar{\omega}_2$of quantum *fcc*-LaH_{10} in Ref. 12 at V' of 35.23, 32.97 and 30.36 Å^3/f.u. and deriving the $\beta(V)$ by inverse volume weight interpolation of neighboring $\beta(V')$;
4. Calculating $\lambda(V)$ in $LaH_{9.63}$ using the estimated $\zeta(V)$ of $LaH_{9.63}$ and the $\beta(V)$ of quantum *fcc*-LaH_{10}.

Critical temperature of superconductivity, T_c

The T_c was evaluated using the Allen–Dynes-modified McMillan equation (AD)[24],

$$T_c = \frac{f_1 f_2 \omega_{log}}{1.2} exp\left[\frac{-1.04(1+\lambda)}{\lambda-\mu^*(1+0.62\lambda)}\right],$$

where f_1 and f_2 are the 'strong-coupling correction' and 'shape correction' factors for strong-coupling systems:

$$f_1 = [1 + (\lambda/\Lambda_1)^{3/2}]^{1/3} \text{ with } \Lambda_1 = 2.46(1 + 3.8\mu^*);$$

$$f_2 = 1 + \left(\bar{\omega}_2/\omega_{log} - 1\right)\lambda^2/\left(\lambda^2 + \Lambda_2^2\right) \text{ with } \Lambda_2 = 1.82(1 + 6.3\mu^*)\left(\bar{\omega}_2/\omega_{log}\right).$$

μ* is the Coulomb coupling constant, which is set to a typical value of 0.1 in this wok.

Structural information of static $LaH_{10-\delta}$.

The simulation cells of *fcc*-LaH_9 (320 atoms) and *fcc*-LaH_{10} (352 atoms) are initialized by a 2×2×2 extension of the unit cell of *F*-43*m*-LaH_9[13] and *Fm*-3*m*-LaH_{10}[12], respectively. We initialize the $LaH_{9.63}$ structure (340 atoms) by adding randomly 20 H atoms to the simulation cell of *fcc*-LaH_9, constraining neighboring vacancies to be no less than 4.4 Å apart to ensure an approximately uniform vacancy distribution, as shown in Supplementary Figure 11. A PIMD simulation (2000 steps) was always carried out on the initial structure to prepare the pre-equilibrium state for the CMD simulation. Vacancy diffusion generally results in a random distribution of vacancies on the 8c and 32f Wyckoff position in *Fm*-3*m*-LaH_{10} within several hundred PIMD steps. The static *P*1-$LaH_{9.63}$, mimicking the quantum fluxional $LaH_{9.63}$, is built by scaling the lattice parameter *a* of a QFS sampled from the CMD simulation of $LaH_{9.63}$ at 176 GPa. The initial vacancy structure of $LaH_{9.63}$ and static *P*1-$LaH_{9.63}$ at 150 GPa can be found at the link—https://doi.org/10.6084/m9.figshare.20484420.v1.

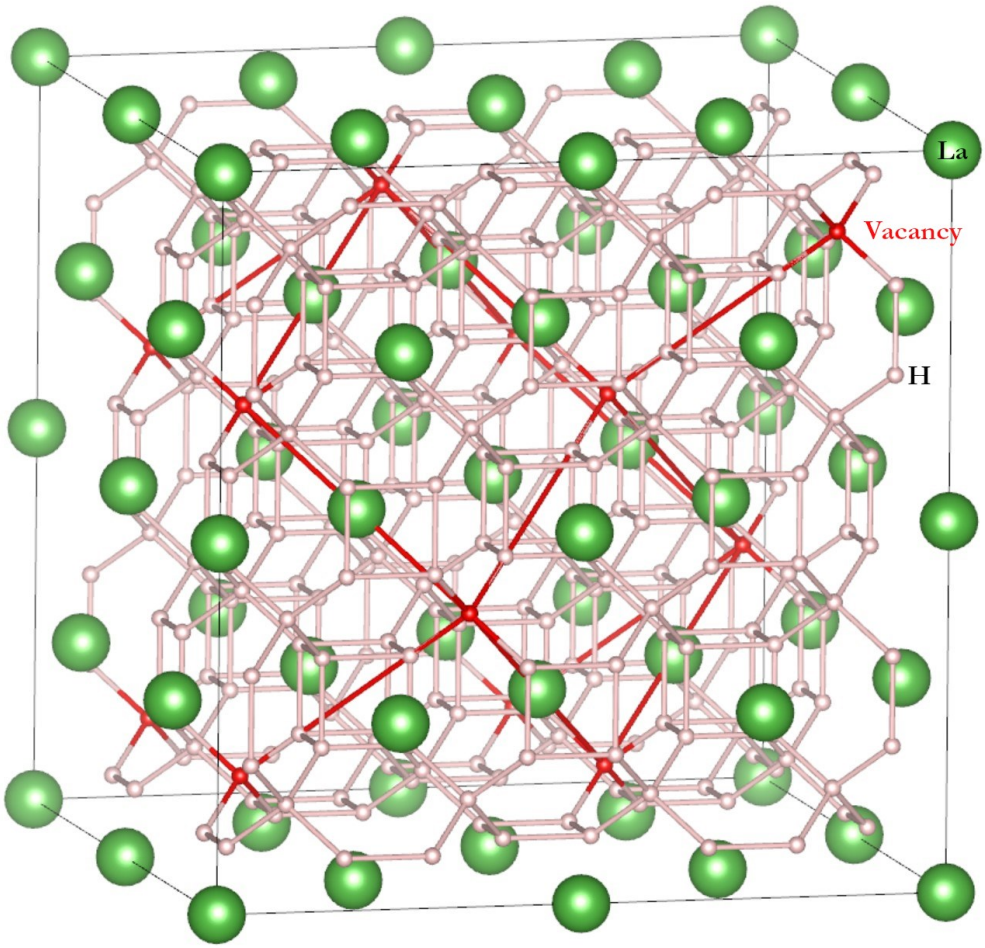

Supplementary Figure 11. Initial vacancy structure of $LaH_{9.63}$.

Supplementary References

(Repeating citations for some references of the main text)

1. Drozdov AP, *et al.* Superconductivity at 250 K in lanthanum hydride under high pressures. *Nature* **569**, 528-531 (2019).

2. Somayazulu M, *et al.* Evidence for Superconductivity above 260 K in Lanthanum Superhydride at Megabar Pressures. *Phys Rev Lett* **122**, 027001 (2019).

3. Struzhkin V, *et al.* Superconductivity in La and Y hydrides: Remaining questions to experiment and theory. *Mat Rad Extr* **5**, 028201 (2020).

4. Kong P, *et al.* Superconductivity up to 243 K in the yttrium-hydrogen system under high pressure. *Nat Commun* **12**, 5075 (2021).

5. Snider E, *et al.* Synthesis of Yttrium Superhydride Superconductor with a Transition Temperature up to 262 K by Catalytic Hydrogenation at High Pressures. *Phys Rev Lett* **126**, 117003 (2021).

6. Ma L, *et al.* High-Temperature Superconducting Phase in Clathrate Calcium Hydride CaH_6 up to 215 K at a Pressure of 172 GPa. *Phys Rev Lett* **128**, 167001 (2022).

7. Peng F, Sun Y, Pickard CJ, Needs RJ, Wu Q, Ma Y. Hydrogen Clathrate Structures in Rare Earth Hydrides at High Pressures: Possible Route to Room-Temperature Superconductivity. *Phys Rev Lett* **119**, 107001 (2017).

8. Liu H, Naumov II, Hoffmann R, Ashcroft NW, Hemley RJ. Potential high-T_c superconducting lanthanum and yttrium hydrides at high pressure. *Proc Natl Acad Sci USA* **114**, 6990 (2017).

9. Liu L, Wang C, Yi S, Kim KW, Kim J, Cho J-H. Microscopic mechanism of room-temperature superconductivity in compressed LaH_{10}. *Phys Rev B* **99**, 140501 (2019).

10. Wang C, Yi S, Cho J-H. Pressure dependence of the superconducting transition temperature of compressed LaH_{10}. *Phys Rev B* **100**, 060502 (2019).

11. Quan Y, Ghosh SS, Pickett WE. Compressed hydrides as metallic hydrogen superconductors. *Phys Rev B* **100**, 184505 (2019).

12. Errea I, *et al.* Quantum crystal structure in the 250-kelvin superconducting lanthanum hydride. *Nature* **578**, 66-69 (2020).

13. Kruglov IA, *et al.* Superconductivity of LaH_{10} and LaH_{16} polyhydrides. *Phys Rev B* **101**, 024508 (2020).

14. Wang H, Tse JS, Tanaka K, Iitaka T, Ma Y. Superconductive sodalite-like clathrate calcium hydride at high pressures. *Proc Natl Acad Sci USA* **109**, 6463 (2012).

15. Xie H, *et al.* High-temperature superconductivity in ternary clathrate $YCaH_{12}$ under high pressures. *J Phys: Condens Matter* **31**, 245404 (2019).

16. Song H, Zhang Z, Cui T, Pickard CJ, Kresin VZ, Duan D. High T_c superconductivity in heavy Rare Earth Hydrides. *Chin Phys Lett* **38**, 107401 (2021).

17. Shiga M, Tachikawa M, Miura S. A unified scheme for ab initio molecular orbital theory and path integral molecular dynamics. *J Chem Phys* **115**, 9149-9159 (2001).

18. Kresse G, Furthmüller J. Efficient iterative schemes for ab initio total-energy calculations using a plane-wave basis set. *Phys Rev B* **54**, 11169-11186 (1996).

19. Pickard CJ, Needs RJ. Structure of phase III of solid hydrogen. *Nat Phys* **3**, 473-476 (2007).

20. Birch F. Finite Elastic Strain of Cubic Crystals. *Phys Rev* **71**, 809-824 (1947).

21. Zhu L*, et al.* A fingerprint based metric for measuring similarities of crystalline structures. *J Chem Phys* **144**, 034203 (2016).

22. Blöchl PE. Projector augmented-wave method. *Phys Rev B* **50**, 17953-17979 (1994).

23. Boeri L. Understanding Novel Superconductors with Ab Initio Calculations. In: *Handbook of Materials Modeling: Applications: Current and Emerging Materials* (eds Andreoni W, Yip S). Springer International Publishing (2018).

24. Allen PB, Dynes RC. Transition temperature of strong-coupled superconductors reanalyzed. *Phys Rev B* **12**, 905-922 (1975).

25. McMillan WL. Transition Temperature of Strong-Coupled Superconductors. *Phys Rev* **167**, 331-344 (1968).